Perturbation Observer based Fractional-order PID Control of Photovoltaics Inverters for Solar Energy Harvesting via Yin-Yang-Pair Optimization

Bo Yang [1], Tao Yu [2,3,*], Hongchun Shu [1], Dena Zhu [1], Fang Zeng [1], Yiyan Sang [4], and Lin Jiang [4]

[1] Faculty of Electric Power Engineering, Kunming University of Science and Technology, 650500 Kunming, China;

[2] College of Electric Power, South China University of Technology, 510640 Guangzhou, China;

[3] Guangdong Key Laboratory of Clean Energy Technology, 510640 Guangzhou, China;

[4] Department of Electrical Engineering & Electronics, University of Liverpool, Liverpool, L69 3GJ, United Kingdom;

* Correspondence: taoyu1@scut.edu.cn, Tel.: +86-130-020-88518

Abstract: In this paper, a novel perturbation observer based fractional-order PID (PoFoPID) control scheme is proposed for a grid-connected Photovoltaics (PV) inverter to harvest the available maximum solar energy from the PV arrays under various atmospheric conditions. A high-gain state and perturbation observer (HGSPO) is adopted to efficiently estimate the aggregated effect of PV inverter nonlinearities, parameter uncertainties, unmodelled dynamics, stochastic fluctuation of atmospheric conditions, and external disturbances. Then, a fractional-order PID (FoPID) control is employed to fully compensate the perturbation estimate and to significantly improve the dynamical responses of the closed-loop system, in which Yin-Yang-Pair optimization (YYPO) algorithm is used to rapidly and effectively seek its optimal control parameters. Inspiringly, PoFoPID control can simultaneously own the elegant merits of global control consistency and robustness of perturbation observer based control, high reliability and simple structure of FoPID control, as well as the global optimality of YYPO algorithm. Four case studies including the solar irradiation change, temperature variation, power grid voltage drop, and inverter parameter uncertainties are undertaken. Simulation results verify the effectiveness and superiority of the PoFoPID control compared to that of PID control, FoPID control, feedback linearization control (FLC), and sliding-mode control (SMC), respectively. At last, a dSpace based hardware-in-loop (HIL) experiment is carried out to validate the implementation feasibility of PoFoPID control.

Keywords: solar energy harvesting; PV inverter; perturbation observer based fractional-order PID control; Yin-Yang-Pair optimization; hardware-in-loop experiment

Nomenclature

Variables		Abbreviations	
V_{dc}	PV output voltage	MPPT	maximum power point tracking
I_{pv}	PV output current	PV	Photovoltaics
I_{ph}	cell's photocurrent	HGPO	high-gain perturbation observer
I_S	cell's reverse saturation current	HGSPO	high-gain state and perturbation observer
I_{RS}	cell's reverse saturation current at reference temperature and solar irradiation	PoFoPID	perturbation observer based fractional-order PID control
T_c	cell's absolute working temperature, K	YYPO	Yin-Yang-Pair optimization
T_{ref}	cell's reference temperature, K	SVPWM	space vector pulse width modulation
S	total solar irradiation, W/m^2	PID	proportional-integral-derivative
E_g	bang-gap energy of the semiconductor used in the cell	FLC	feedback linearization control
$v_{d,q}$	d-q components of the output voltage of the inverter	FoPID	fractional-order proportional-derivative
$e_{d,q}$	d-q components of the grid voltage	HIL	hardware-in-loop
$i_{d,q}$	d-q components of the grid current	SMC	Sliding-mode control
ω	AC grid synchronous frequency	INC	incremental conductance
System parameters		The control parameters of POFO-SMC	
q	electron charge, $1.60217733 \times 10^{-19}$ Cb	α_i	Luenberger observer gains
A	p-n junction ideality factor, between 1 and 5	ϵ_i	observer constant
k	Boltzman's constant, 1.380658×10^{-23} J/K	B_0	constant control gain matrix
k_i	cell's short-circuit current temperature coefficient	K_{Pi}	proportional gain
R_s	cell series resistance	K_{Ii}	integral gain
N_p	number of panels connected in parallel	K_{Di}	derivative gain
N_s	number of panels connected in series	λ_i	fractional differentiator order
V_N	output voltage of the PV array at the Nth sample of time	μ_i	fractional integrator order
R	equivalent grid resistance in dq frame	I_{min}, I_{max}	minimum/maximum number of archive updates
L	equivalent grid inductance in dq frame	α	expansion/contraction factor
C	DC bus capacitance	δ_1, δ_2	corresponding search radii in the splitting

1. Introduction

Environmental problems, e.g., greenhouse gas emission, rising temperature, accelerated plant cover melting, which were once insignificant and local in the middle of the twentieth century, are now evolving into a severe issue in the global scale and are astonishingly threatening all living creatures and the whole human society. Such notorious issues are mainly resulted from the massive use of fast-depleting fossil fuels including coal, oil, and natural gas [1]. In order to tackle the ubiquitous environmental challenges and the ever-growing energy crisis, dramatic concerns about renewable energy resources (RES) have been urgently raised for the sake of a clean and sustainable future of the modern world [2].

Among different types of RES, growing attentions have been focused on solar energy thanks to its elegant features of abundance of solar resources, ease of device installation, noiseless and safe operation with relatively low operation costs [3]. In practice, the generated DC currents from the solar cell are usually converted into AC currents through Photovoltaics (PV) inverter before connecting to the power grids or local utilizers [4]. Generally speaking, the voltage generated by the PV system is relatively low due to its nonlinear nature which might be inadequate for different load applications. In order to increase the generation efficiency, maximum power point tracking (MPPT) techniques [5] are often adopted, which attempt to track the maximum operation point from the PV panel in the presence of changing solar irradiance or temperature [6]. Some typical MPPT algorithms can be referred to perturb & observe (P&O) [7], incremental conductance (INC) [8], particle swarm optimization (PSO) [9], cuckoo search (CS) [10], neural network (NN) [11], etc.

After the maximum power point (MPP) is obtained by the MPPT algorithm, an important task is how to effectively track the DC-link voltage reference by the PV inverter, such that the MPPT could be finally realized. As a result, a proper PV inverter controller that owns a fast dynamic response, robustness to disturbances, small tracking error, and low total harmonic distortion needs to be designed [12]. Conventional vector control (VC) [13,14] associated with proportional-integral-derivative (PID) loops is widely used for PV inverters control system design as it offers simple structure, easy implementation, and high reliability. In order to improve the control performance of PID control, fractional-order PID (FoPID) control schemes have been adopted based on fractional calculus, which introduce two additional parameters, e.g., fractional integrator and fractional differentiator to significantly enhance the dynamical performance [15]. For example, a minimal-energy control of an uncertain-parameter oriented PV system was developed with a half-order PID control to enhance the robustness of the PV system [16]. Besides, various meta-heuristic optimization algorithms were employed to seek the optimal FoPI control parameters of on-gird solar PV systems [17]. However, the control performance of the above methods will be inevitably degraded when operation conditions vary as their control parameters are determined by one-point linearization. Such inherent weakness grows to be quite severe for the PV inverter due to the fast and stochastic time-varying variation of atmospheric conditions.

On the other hand, an enormous variety of nonlinear controllers have been designed to handle the aforementioned essential flaws of the linear controllers. In work [18,19], feedback linearization control (FLC) was proposed for a two-level and a three-level grid-connected PV inverter to achieve MPPT, respectively. Nevertheless, it requires an accurate PV inverter model, which lacks of robustness to parameter or modelling uncertainties. To remedy this disadvantage, a robust partial feedback linearizing stabilization scheme [20] was designed, which guarantees the stability for all possible disturbances within the given upper bounds of the modelling errors based on the satisfaction of matching condition. Moreover, literature [21] devised an improved double integral sliding mode MPPT controller (IDISMC) for a stand-alone PV system, in which the parameters of solar panels model were estimated by genetic algorithm (GA). In addition, a backstepping based nonlinear MPPT controller was developed which can achieve a fast dynamical response [22]. Furthermore, in work [23], model predictive control (MPC) was presented for marine PV system, such that a considerable robustness could be realized. Besides, a disturbance estimator based predictive current controller was used in [24] to simultaneously handle the unmodelled dynamics and parameter uncertainties of PV systems.

Undoubtedly, disturbances and uncertainties widely exist in all industrial systems that often bring adverse effects on the performance or even the stability of control systems. Therefore, numerous disturbance/perturbation observer based control schemes have been developed which attempt to reject the malignant effects of various uncertainties and to improve robustness [25]. In fact, they are quite promising for PV inverter control as the PV system parameter uncertainties and atmospheric uncertainties are quite common and frequent in their operation. Based on the above discussions, this paper aims to propose a novel perturbation observer based fractional-order PID (PoFoPID) control for a grid-connected PV inverter to achieve MPPT under various atmospheric conditions, which control parameters are optimally tuned by a meta-heuristic algorithm called Yin-Yang-Pair optimization (YYPO) [26-28]. YYPO is motivated from the fact that many aspects in the universe are determined by dualities, which is not based on any specific mechanism or physical event but is designed to explicitly balance the

exploration and exploitation thus attempts to be a realization of the Yin-Yang philosophy of balance between conflicting forces.

The contribution and novelty of this paper can be summarized as follows:

● *Significant robustness*: The PV inverter nonlinearities and parameter uncertainties, unmodelled dynamics, stochastic fluctuation of atmospheric conditions, and external disturbances are aggregated into a perturbation, which is then rapidly estimated online by a high-gain state and perturbation observer (HGSPO) [29-31] and is fully compensated by the controller. Thus, PoFoPID control can handle various uncertainties and a great robustness can be achieved;

● *Satisfactory control performance*: Compared to conventional PID control, PoFoPID control can dramatically improve the dynamical responses of the closed-loop system by the introduction of two additional fractional orders. Compared to FoPID control, PoFoPID control can achieve a globally control consistency thanks to the full perturbation compensation. Compared to FLC, PoFoPID control can provide great robustness as it does not require an accurate PV system model. Compared to SMC, PoFoPID control can avoid the over-conservative control performance of SMC as the real-time perturbation estimate is used instead of the upper bound of perturbation.

● *Efficient optimization*: Unlike other meta-heuristic algorithms which are based on a specific natural/physical phenomenon, YYPO algorithm is designed explicitly to balance the exploitation and exploration associated with simple mechanism. Hence, it can rapidly seek the optimal PoFoPID control parameters and an optimal control performance can be ensured;

● *Justified implementation*: A dSpace based hardware-in-loop (HIL) experiment is undertaken, which validates the implementation feasibility of PoFoPID control.

The remaining of this paper is organized as follows: Section 2 aims to model the grid-connected PV inverter. Section 3 designs the PoFoPID control design via YYPO. In Section 4, PoFoPID control is applied on the PV inverter to achieve MPPT. Comprehensive case studies and HIL experiment are provided in Section 5 and Section 6, respectively. Some discussions about YYPO are provided in Section 7. At last, Section 8 concludes the whole paper.

2. Modelling of Grid-connected PV Inverter

Figure 1 depicts the configuration of a PV inverter connected to the power grid, which includes a PV array, a DC-link capacitor, a three-phase two-level inverter and a three-phase power grid. The PV array attempts to convert the solar irradiation into the DC current, while the DC-link capacitor aims to reduce the high-frequency ripples of the DC voltage [6].

2.1. PV array modelling

In general, a PV cell is a p-n semiconductor junction diode that converts solar energy into electricity. It is consisted of a light generated current source, a parallel diode, and a series resistance, respectively. PV cells are normally grouped together to form PV modules, which are combined in both series and parallel to offer a desired output power [20]. Denote the number of cells in series and in parallel to be N_s and N_p, respectively, the relationship between the output current and the voltage is written as [18,19]

$$I_{pv} = N_p I_{ph} - N_p I_s \left(\exp\left[\frac{q}{AKT_c} \left(\frac{V_{dc}}{N_s} + \frac{R_s I_{pv}}{N_p} \right) \right] - 1 \right) \tag{1}$$

where the meaning of each symbol is given in Nomenclature.

The generated photocurrent I_{ph} is given as

$$I_{ph} = \left(I_{sc} + k_i (T_c - T_{ref}) \right) \frac{s}{1000} \tag{2}$$

Moreover, the cell's saturation current I_s varies with the temperature according to the following equation:

$$I_s = I_{RS} \left[\frac{T_c}{T_{ref}} \right]^3 \exp\left[\frac{q E_g}{Ak} \left(\frac{1}{T_{ref}} - \frac{1}{T_c} \right) \right] \tag{3}$$

The reverse saturation current at the rated temperature and solar irradiation is approximated as

$$I_s = \frac{I_{sc}}{\exp\left(\frac{q V_{oc}}{N_s k A T_c} \right) - 1} \tag{4}$$

The above equations (1)-(4) show that the current generated by the PV array depends on the temperature and solar irradiation.

2.2 PV inverter modelling

Only the balanced conditions are taken into account, e.g., the three phases have identical parameters and their voltages and currents have the same amplitude while each phase shifts 120° between themselves. The PV inverter dynamics under the synchronous rotating *dq* frame can be obtained through Park's transformation, as follows [18]
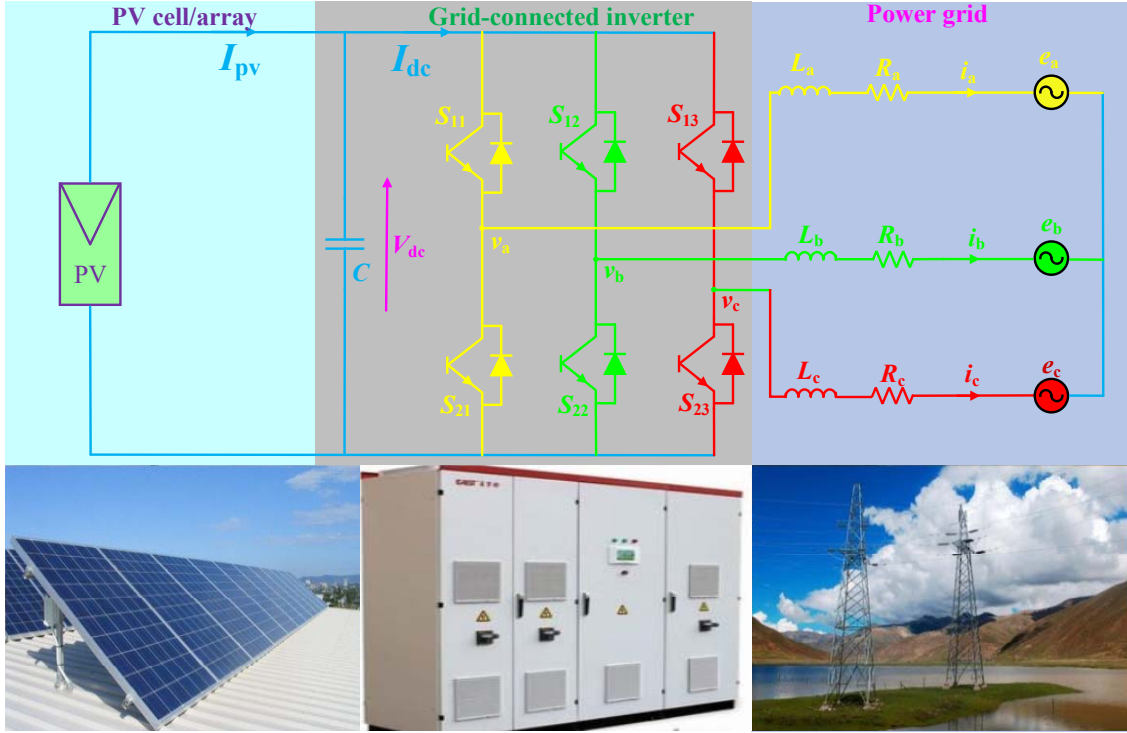
Figure 1. Configuration of a grid-connected PV inverter.

$$\begin{cases} v_\mathrm{d} = e_\mathrm{d} + Ri_\mathrm{d} + L\dfrac{di_\mathrm{d}}{dt} + \omega Li_\mathrm{q} \\ v_\mathrm{q} = e_\mathrm{q} + Ri_\mathrm{q} + L\dfrac{di_\mathrm{q}}{dt} - \omega Li_\mathrm{d} \end{cases} \tag{5}$$

where e_d, e_q, i_d, i_q, v_d, and v_q denote the dq-axis components of grid voltage, grid current, and inverter output voltage, respectively; L and R represent the equivalent grid inductance and grid resistance, respectively; and ω means the AC grid synchronous frequency. Here, the switching power losses produced in the PV inverter is ignored, then the power balance between the DC input side and the AC output side is described by

$$e_\mathrm{d}i_\mathrm{d} + e_\mathrm{q}i_\mathrm{q} = V_{dc}I_{dc} \tag{6}$$

where I_{dc} and V_{dc} are the current and voltage across the DC-link capacitor, respectively.

At last, the DC-link dynamics is obtained by applying Kirchhoff's current law, as follows:

$$C\frac{dV_{dc}}{dt} = I_{pv} - I_{dc} = I_{pv} - \frac{e_\mathrm{d}i_\mathrm{d} + e_\mathrm{q}i_\mathrm{q}}{V_{dc}} \tag{7}$$

where C denotes the DC-link capacitor.

2.3 INC based MPPT technique

The PV systems are required to always operate at the maximum output level due to their inherent low efficiency [6]. Figure 2 provides the current-voltage (*I-V*) and power-voltage (*P-V*) curves for different solar irradiation and different temperature. Figure 2(a) shows that a higher solar irradiation results in an increase of the generated current while Figure 2 (b) illustrates that a higher temperature leads to a growth of that current. Besides, Figure 2 (c) demonstrates that a lower solar irradiation leads to a decrease of the generated power while Figure 2 (d) presents that a lower temperature causes an increase for that power. For any given set of operational conditions, PV cells have a single operation point where the values of the current (*I*) and voltage (*V*) of the PV cell result in a maximum power output. A PV cell, for the majority of its useful curve, acts as a constant current source (lower than 350 V), as shown in the *I-V* curve of Fig. 2 (a),(b). However, at a PV cell's MPP region, its curve has an approximately inverse exponential relationship between current and voltage. From basic circuit theory, the power delivered from or to a device is optimized where the derivative (graphically, the slope) d*I*/d*V* of the *I-V* curve is equal and opposite to the *I/V* ratio (where d*P*/d*V*=0). This is known as the maximum power point (MPP) and corresponds to the 'knee' of the curve, as shown in the *P-V* curve of Fig. 2 (c),(d). In practice, MPPT is a powerful technique that attempts to dynamically adjust the output voltage of the PV array for available maximum solar energy harvesting at different levels of temperature or solar irradiation. Since the power efficiency of PV modules available in the market is low, it is required that the PV modules should always operate at the MPP.

INC technique [8] is applied to efficiently track the MPP under the rapid time-varying atmospheric conditions. Basically, it follows the fact that the derivative of output power with respect to output voltage is zero at MPP, positive at the left side of MPP while negative at the right side of MPP, as follows:

$$\begin{cases} \frac{\Delta I}{\Delta V} = -\frac{I}{V}, & \text{at MPP} \\ \frac{\Delta I}{\Delta V} > -\frac{I}{V}, & \text{left side of MPP} \\ \frac{\Delta I}{\Delta V} < -\frac{I}{V}, & \text{right side of MPP} \end{cases} \tag{8}$$

where $\Delta I/\Delta V$ denotes the incremental conductance and I/V represents the instantaneous conductance.
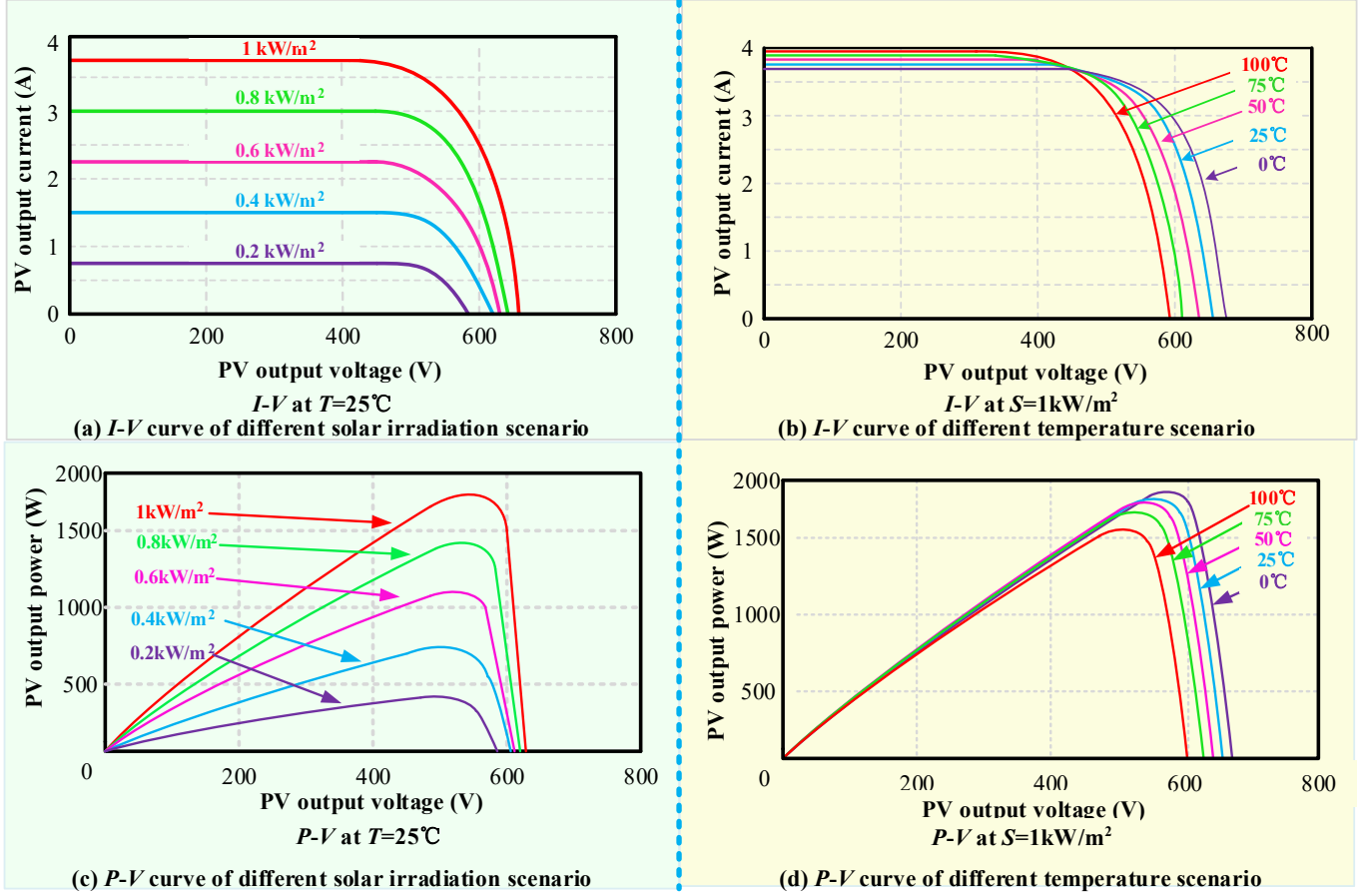

Figure 2. Current-voltage and power-voltage characteristics of PV array obtained under different solar irradiation scenario and different temperature scenario.

3 Perturbation Observer based Fractional-order PID Control Design via Yin-Yang-Pair Optimization

This section aims to design PoFoPID control for PV systems to achieve MPPT. Compared to other meta-heuristic algorithms, YYPO is employed for parameter tuning which owns the advantages of simple algorithm structure and proper trade-off between exploitation and exploration. Compared to other typical control schemes, PoFoPID control has the advantage of improved dynamic responses against PID control, global control consistency against FoPID control, great robustness against FLC, and more reasonable control performance against SMC.

3.1 High-gain state and perturbation observer

Consider an uncertain nonlinear system that has the following canonical form

$$\begin{cases} \dot{x} = Ax + B(a(x) + b(x)u + d(t)) \\ y = x_1 \end{cases} \tag{9}$$

where $x = [x_1, x_2, \cdots, x_n]^{\text{T}} \in \mathcal{R}^n$ represents the state variable vector; $y \in \mathcal{R}$ and $u \in \mathcal{R}$ denote the system output and control input, respectively; $a(x): \mathcal{R}^n \mapsto \mathcal{R}$ and $b(x): \mathcal{R}^n \mapsto \mathcal{R}$ are some unknown smooth functions; and $d(t): \mathcal{R}^+ \mapsto \mathcal{R}$ represents a time-varying external disturbance, respectively. The matrix A and matrix B are of the canonical form as follows:

$$A = \begin{bmatrix} 0 & 1 & 0 & \cdots & 0 \\ 0 & 0 & 1 & \cdots & 0 \\ \cdots & \cdots & \cdots & \cdots & \cdots \\ 0 & 0 & 0 & \cdots & 1 \\ 0 & 0 & 0 & \cdots & 0 \end{bmatrix}_{n \times n}, B = \begin{bmatrix} 0 \\ 0 \\ \vdots \\ 0 \\ 1 \end{bmatrix}_{n \times 1} \tag{10}$$

The perturbation of system (13) is defined as [29-31]

$$\psi(x, u, t) = a(x) + (b(x) - b_0)u + d(t) \tag{11}$$

where b_0 is the constant control gain.

For the original system (9), the last state x_n can be rewritten in the presence of perturbation (11), which yields

$$\dot{x}_n = a(x) + (b(x) - b_0)u + d(t) + b_0 u = \psi(x, u, t) \tag{12}$$

Define a *fictitious* state to represent the perturbation, e.g., $x_{n+1} = \psi(x, u, t)$. Then, system (9) can be directly extended into

$$\begin{cases} y = x_1 \\ \dot{x}_1 = x_2 \\ \quad\vdots \\ \dot{x}_n = x_{n+1} + b_0 u \\ \dot{x}_{n+1} = \dot{\psi}(\cdot) \end{cases} \tag{13}$$

The new state vector becomes $x_e = [x_1, x_2, \cdots, x_n, x_{n+1}]^T$. Throughout this paper, $\tilde{x} = x - \hat{x}$ refers to the estimation error of x whereas $\hat{x}$ represents the estimate of x, while x^* denotes the reference of variable x. The assumptions made on perturbation and their role can be referred to literatures [29-31]. Consider the worst case, e.g., $y=x_1$ is the only measurable state, an $(n+1)$th-order HGSPO for the extended system (13) is used to simultaneously estimate the states and perturbation by [29-31]

$$\dot{\hat{x}}_e = A_0 \hat{x}_e + B_1 u + H(x_1 - \hat{x}_1) \tag{14}$$

where observer gain $H = [\alpha_1/\varepsilon, \alpha_2/\varepsilon^2, \dots, \alpha_n/\varepsilon^n, \alpha_{n+1}/\varepsilon^{n+1}]^T$; thickness layer boundary of observer $0 < \varepsilon \ll 1$; and Luenberger observer gains α_i, $i = 1, 2, \cdots, n + 1$, are chosen to place the poles of polynomial $s^{n+1} + \alpha_1 s^n + \alpha_2 s^{n-1} + \cdots + \alpha_{n+1} = (s + \lambda_\alpha)^{n+1} = 0$ being in the open left-half complex plane at $-\lambda_\alpha$, with

$$\alpha_i = C_{n+1}^i \lambda_\alpha^i, i = 1, 2, \cdots, n + 1. \tag{15}$$

The matrix A_0 and B_1 are in the following form:

$$A_0 = \begin{bmatrix} 0 & 1 & 0 & \cdots & 0 \\ 0 & 0 & 1 & \cdots & 0 \\ \cdots & \cdots & \cdots & \cdots & \cdots \\ 0 & 0 & 0 & \cdots & 1 \\ 0 & 0 & 0 & \cdots & 0 \end{bmatrix}_{(n+1)\times(n+1)}, B = \begin{bmatrix} 0 \\ 0 \\ \vdots \\ 0 \\ 1 \end{bmatrix}_{(n+1)\times 1} \tag{16}$$

3.2 Fractional-order PID control

Fractional-order calculus is a generalization of integration and differentiation to non-integer order domain, the fundamental operator $_a\mathrm{D}_t^\alpha$ is defined as [32]

$$_a\mathrm{D}_t^\alpha = \begin{cases} \dfrac{\mathrm{d}^\alpha}{\mathrm{d}t^\alpha}, & \alpha > 0 \\ 1, & \alpha = 0 \\ \int_a^t (\mathrm{d}\tau)^{-\alpha}, & \alpha < 0 \end{cases} \tag{17}$$

where a and t are the lower and upper limits while $\alpha \in \mathcal{R}$ is the operation order.

Here, one of the commonly used definition of fractional-order derivative, e.g., Riemann-Liouville (RL) definition, is used with *Gamma* function, as

$$_a\mathrm{D}_t^\alpha f(t) = \frac{1}{\Gamma(n-\alpha)} \frac{\mathrm{d}^n}{\mathrm{d}t^n} \int_a^t \frac{f(\tau)}{(t-\tau)^{\alpha-n+1}} \mathrm{d}\tau \tag{18}$$

where n is the first integer which is not less than α, e.g., $n - 1 \le \alpha < n$. $\Gamma(\cdot)$ is the *Gamma* function.

The transfer function of FoPID control is given by

$$G(s) = K_P + \frac{K_I}{s^\mu} + K_D s^\lambda \tag{19}$$

where K_P, K_I and K_D are the proportional gain, integral gain, and derivative gain, respectively. In addition, μ and λ (between 0 to 2) denote the fractional integrator order and fractional differentiator order, respectively. The introduction of these two parameters can properly tune the dynamics of many physical systems.

Here, the Oustaloup approximation is adopted to approximate the exact solution of fractional differential equations. This paper chooses the lower limit of frequency $\omega_b = 0.2$ and upper limits of frequency $\omega_h = 5$, while the approximation order $N=3$ [32].

3.3 Yin-Yang-Pair Optimization

YYPO is developed from the ancient Chinese divination text and the oldest of the Chinese classics, called *I Ching* or *The book of Changes*, which can be traced back to more than two and a half millennia and provides inspiration to the worlds of religion, psychoanalysis, business, literature, and art. The *I Ching* employs a type of divination called cleromancy, which produces apparently random numbers. Particularly, six numbers between 6 and 9 are turned into a hexagram which have been often endowed with cosmological meaning. Each hexagram is a figure composed of six stacked horizontal lines, each line is either Yin (broken line) or Yang (unbroken line). The

commonest operators in the process of divination to transform a given hexagram to another are intricate, synthesis, and mutual operator, such that different faces of a face can be represented by the hexagram [26], as shown in Fig. 3.
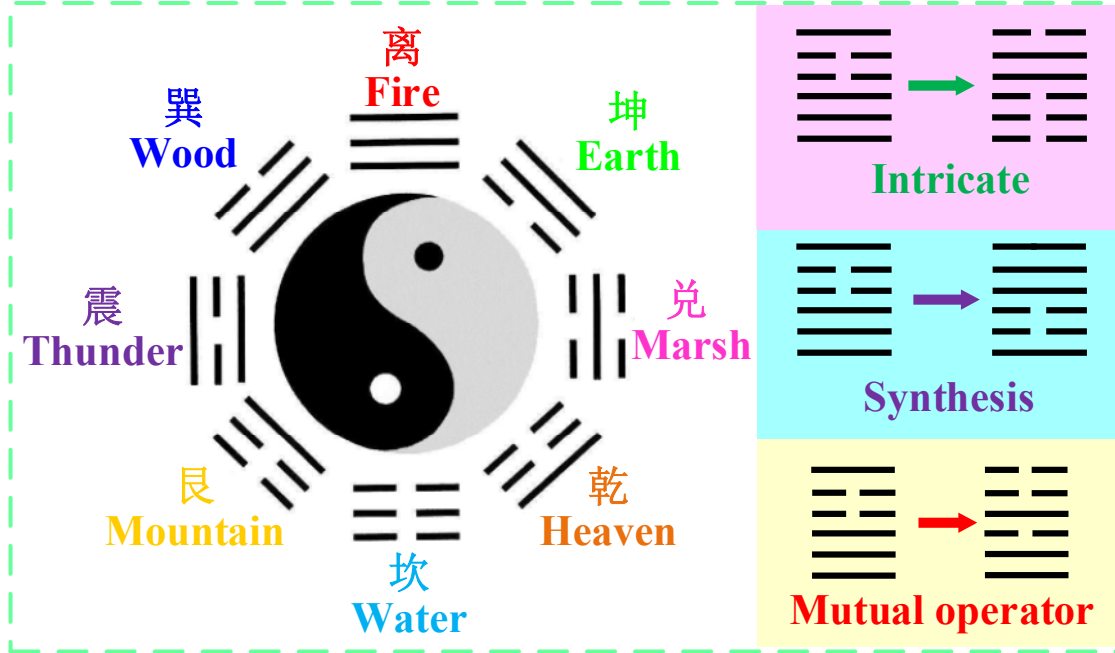

Figure 3. The typical hexagram of *I Ching* with the corresponding representative in nature and commonest operators.

The algorithm begins with the generation of two random points in the domain of $[0,1]^D$ and evaluating their fitness. The fitter one of the two points is nominated as P_1 and the other as P_2. The required parameters in terms of the minimum and maximum number of archive updates (I_{min} and I_{max}) and the expansion/contraction factor (α) need to be specified. The number of archive updates is randomly generated between I_{min} and I_{max}. As a consequence, the iteration loop is initiated and the fitness of the two points are compared. If P_2 is fitter than P_1, the points and their corresponding δ values are interchanged, which ensures that the iteration starts with the fitter point as P_1. There are two stages for YYPO which are briefly summarized as follows, more details can be referred to literatures [27,28] for interested readers.

● *Splitting stage*

The inputs to the splitting stage are one of the points (P_1 or P_2) along with its corresponding search radii (δ_1 and δ_2). Although both points experience the splitting stage, only a single point (referred as P) along with its search radii (δ) undergoes the splitting stage at a time. This is implemented by one of the following two methods and is decided based on an equal probability:

One-way splitting: $2D$ identical copies of the point P are stored as S which can be considered as a matrix of size $2D*D$. One variable of each point in S is modified as follows:

$$S_j^j = S^j + r\delta \quad \text{and} \quad S_{D+j}^j = S^j - r\delta, \quad \text{where } j=1,2,3\ldots D \tag{20}$$

where the subscript denotes the point number whereas the superscript denotes the decision variable number that is being modified while r means a random number between 0 and 1, respectively.

D-way splitting: $2D$ identical copies of the point P are stored as S which can be considered as a matrix of size $2D*D$. A binary matrix B is generated containing $2D$ random binary strings of length D such that each string is unique. Hence, every variable of each point is modified by

$$S_k^j = S^j + r(\frac{\delta}{\sqrt{2}}) \quad \text{if} \quad B_k^j = 1, S_k^j = S^j + r(\frac{\delta}{\sqrt{2}}) \quad \text{else,} \quad \text{where } k=1,2,3,\ldots2D \text{ and } j=1,2,3\ldots D \tag{21}$$

● *Archive stage*

The archive stage is initiated after the required number of archive updates have been reached and it is to be noted that the archive contains $2I$ points at this stage, corresponding to the two points (P_1 or P_2) being added at each update before the splitting stage, as follows:

$$\begin{cases} \delta_1 = \delta_1 - \left(\frac{\delta_1}{\alpha}\right) \\ \delta_2 = \delta_2 - \left(\frac{\delta_2}{\alpha}\right) \end{cases} \tag{22}$$

At the end of the archive stage, the archive matrix is set to null, and a new value for the number of archive updates I is randomly generated within its specified bounds, e.g., I_{min} and I_{max}.

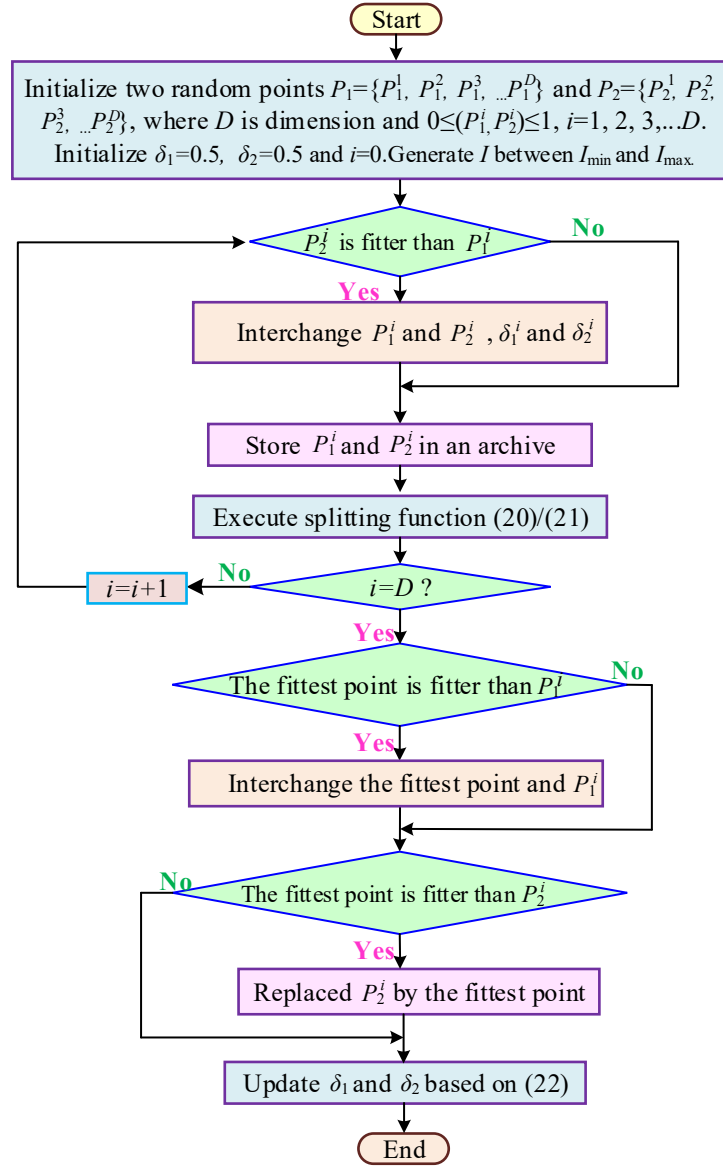The flowchart of YYPO is illustrated in Figure 4.

Figure 4. The flowchart of YYPO.

3.4 Overall PoFoPID control design

The overall PoFoPID control for system (9) is designed as

$$u = \frac{1}{b_0}[x_1^{*(n)} - \hat{\psi}(\cdot) + K_P^*(x_1 - x_1^*) + \frac{K_I^*}{s^{\mu^*}}(x_1 - x_1^*) + K_D^* s^{\lambda^*}(x_1 - x_1^*)] \tag{23}$$

where x_1^* denotes the reference of state x_1. $K_P^*, K_I^*, K_D^*, \mu^*,$ and λ^* are the optimal PoFoPID control parameters obtained by YYPO.

The overall design procedure of PoFoPID control for system (9) can be summarized as follows:

Step 1: Define perturbation (11) for the original nth-order system (9);

Step 2: Employ an extended state $x_{n+1} = \psi(\cdot)$ to represent perturbation (11);

Step 3: Extend the original nth-order system (9) into the extended $(n+1)$th-order system (13);

Step 4: Use the $(n+1)$th-order HGSPO (14) for the extended $(n+1)$th-order system (13);

Step 5: Design PoFoPID control (23) for the original nth-order system (9), which optimal control parameters are obtained through YYPO (20)-(22).

4 PoFoPID Control Design of PV Inverter

For PV system (1)-(7), define the state vector as $x = (x_1, x_2, x_3)^T = (i_d, i_q, V_{dc})^T$, system output $y = (y_1, y_2)^T = (i_q, V_{dc})^T$, and control input $u = (u_1, u_2)^T = (v_d, v_q)^T$, respectively.

Differentiate the output y until control input u appears explicitly, yields

$$\begin{bmatrix} \dot{y}_1 \\ \ddot{y}_2 \end{bmatrix} = \begin{bmatrix} -\frac{R}{L}i_q + \omega i_d - \frac{e_q}{L} \\ \frac{i_{pv}}{C} - \frac{e_d\left(-\frac{R}{L}i_d - \omega i_q - \frac{e_d}{L}\right) + e_q\left(-\frac{R}{L}i_q + \omega i_d - \frac{e_q}{L}\right)}{CV_{dc}} - \frac{(e_d i_d + e_q i_q)}{C^2 V_{dc}^2}I_{pv} + \frac{(e_d i_d + e_q i_q)^2}{C^2 V_{dc}^3} \end{bmatrix} + B(x)\begin{bmatrix} u_1 \\ u_2 \end{bmatrix} \qquad (24)$$

with

$$B(x) = \begin{bmatrix} 0 & \frac{1}{L} \\ -\frac{e_d}{LCV_{dc}} & -\frac{e_q}{LCV_{dc}} \end{bmatrix} \qquad (25)$$

In order to ensure the above input-output linearization to be valid, the control gain matrix $B(x)$ must be nonsingular among the whole operation range, which requires

$$\det[B(x)] = \frac{e_d}{L^2 CV_{dc}} \neq 0 \qquad (26)$$

As the d-axis component of grid voltage e_d is always different from zero, the above condition can be always satisfied.

Assume all the nonlinearities and parameters of PV systems are unknown, define the perturbations $\psi_1(\cdot)$ and $\psi_2(\cdot)$ for PV system (24), as follows:

$$\begin{bmatrix} \psi_1(\cdot) \\ \psi_2(\cdot) \end{bmatrix} = \begin{bmatrix} -\frac{R}{L}i_q + \omega i_d - \frac{e_q}{L} \\ \frac{i_{pv}}{C} - \frac{e_d\left(-\frac{R}{L}i_d - \omega i_q - \frac{e_d}{L}\right) + e_q\left(-\frac{R}{L}i_q + \omega i_d - \frac{e_q}{L}\right)}{CV_{dc}} - \frac{(e_d i_d + e_q i_q)}{C^2 V_{dc}^2}I_{pv} + \frac{(e_d i_d + e_q i_q)^2}{C^2 V_{dc}^3} \end{bmatrix} + (B(x) - B_0)\begin{bmatrix} u_1 \\ u_2 \end{bmatrix} \qquad (27)$$

with the constant control gain matrix B_0 being given by

$$B_0 = \begin{bmatrix} b_{11} & 0 \\ 0 & b_{22} \end{bmatrix} \qquad (28)$$

where b_{11} and b_{22} are the constant control gains. Here, matrix B_0 is chosen in the diagonal form to fully decouple the control of q-axis current i_q and DC-link voltage V_{dc}.

Define the tracking error $e = [e_1, e_2]^T = [i_q - i_q^*, V_{dc} - V_{dc}^*]^T$, where q-axis current reference i_q^* is given by power grid operators or utilizers while DC-link voltage reference V_{dc}^* is determined by INC based MPPT technique (8). Differentiate the tracking error e until the control input u appears explicitly, it gives

$$\begin{bmatrix} \dot{e}_1 \\ \ddot{e}_2 \end{bmatrix} = \begin{bmatrix} \psi_1(\cdot) \\ \psi_2(\cdot) \end{bmatrix} + B_0\begin{bmatrix} u_1 \\ u_2 \end{bmatrix} - \begin{bmatrix} \dot{i}_q^* \\ \ddot{V}_{dc}^* \end{bmatrix} \qquad (29)$$

A second-order high-gain perturbation observer (HGPO) is used to estimate perturbation $\psi_1(\cdot)$ as

$$\begin{cases} \dot{\hat{i}}_q = \hat{\psi}_1(\cdot) + \frac{\alpha_{11}}{\epsilon_1}(i_q - \hat{i}_q) + b_{11}u_1 \\ \dot{\hat{\psi}}_1(\cdot) = \frac{\alpha_{12}}{\epsilon_1^2}(i_q - \hat{i}_q) \end{cases} \qquad (30)$$

where the Luenberger observer gains α_{11} and α_{12} are all positive constants, with $0 < \epsilon_1 \ll 1$.

Meanwhile, a third-order HGSPO is adopted to estimate perturbation $\psi_2(\cdot)$ as

$$\begin{cases} \dot{\hat{V}}_{dc} = \hat{\dot{V}}_{dc} + \frac{\alpha_{21}}{\epsilon_2}(V_{dc} - \hat{V}_{dc}) \\ \dot{\hat{\dot{V}}}_{dc} = \hat{\psi}_2(\cdot) + \frac{\alpha_{22}}{\epsilon_2^2}(V_{dc} - \hat{V}_{dc}) + b_{22}u_2 \\ \dot{\hat{\psi}}_2(\cdot) = \frac{\alpha_{23}}{\epsilon_2^3}(V_{dc} - \hat{V}_{dc}) \end{cases} \qquad (31)$$

where the Luenberger observer gains α_{21}, α_{22} and α_{23} are all positive constants, with $0 < \epsilon_2 \ll 1$.

The PoFoPID control for PV system (24) can now be designed as

$$\begin{bmatrix} u_1 \\ u_2 \end{bmatrix} = B_0^{-1}\begin{bmatrix} \dot{i}_q^* - \hat{\psi}_1(\cdot) + K_{P1}^* e_1 + \frac{K_{I1}^*}{s^{\mu_1^*}}e_1 + K_{D1}^* s^{\lambda_1^*}e_1 \\ \ddot{V}_{dc}^* - \hat{\psi}_2(\cdot) + K_{P2}^* e_2 + \frac{K_{I2}^*}{s^{\mu_2^*}}e_2 + K_{D2}^* s^{\lambda_2^*}e_2 \end{bmatrix} \qquad (32)$$

where optimal control parameters K_{Pi}^*, K_{Ii}^*, K_{Di}^*, λ_i^*, and μ_i^*, with $i=1,2$, are tuned by YYPO under three cases, e.g., (a) Solar irradiation change, (b) Temperature variation, and (c) Power grid voltage drop. The optimization goal is to minimize the tracking error of DC-link voltage and q-axis current and the overall control costs, as follows:

$$\text{Minimize } f = \sum_{\text{Three cases}} \int_0^T (|V_{dc} - V_{dc}^*| + |i_q - i_q^*| + \omega_1|u_1| + \omega_2|u_2|)\,dt$$

$$\text{subject to} \quad \begin{cases} 0 \le K_{Pi} \le 200 \\ 0 \le K_{Ii} \le 400 \\ 0 \le K_{Di} \le 20 \\ 0 \le \lambda_i \le 2 \\ 0 \le \mu_i \le 2 \\ -0.8 \le u_i \le 0.8 \end{cases}, \quad i=1,2. \tag{33}$$

where the weights ω_1 and ω_2 are used to scale the magnitude of control costs which are chosen to be 1/4. T=3 s denotes the simulation time and the control costs are bounded to avoid the admissible capacity of the VSC at some operation points. The user-defined YYPO parameters are chosen from reference [27] as the minimum and maximum number of archive updates to be I_{min}=1 and I_{max}=3, and the expansion/contraction factor α =20, respectively. Moreover, the value of corresponding search radii δ_1 and δ_2 are set at 0.5 while the convergence criteria of YYPO is chosen by

$$|f_k - f_{k-1}| \le \varepsilon \tag{34}$$

where ε is the tolerance of convergence error, which value is chosen to be 10^{-4} in this paper; f_k and f_{k-1} represent the fitness function value calculated at the kth iteration and the (k-1)th iteration, respectively.

Lastly, the overall control structure of PoFoPID (32) for PV system (24) to achieve MPPT is illustrated by Figure 5. Here, only the measurement of q-axis current i_q and DC-link voltage V_{dc} is required.
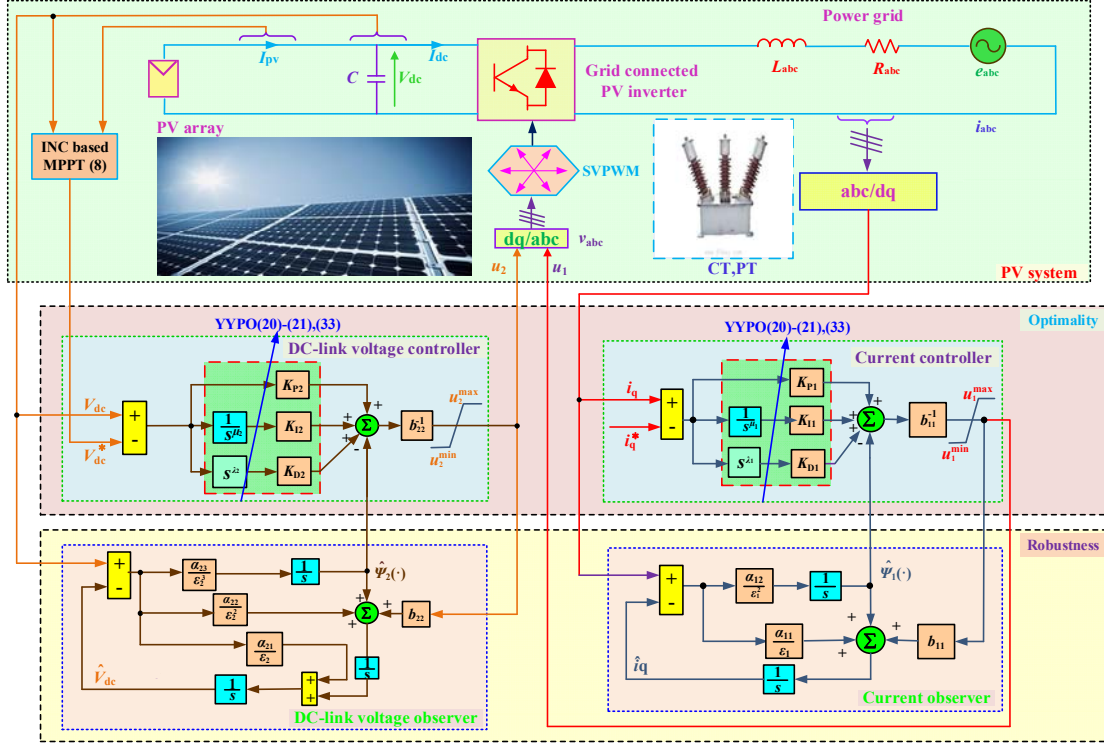

Figure 5. The overall PoFoPID control structure of the grid connected PV inverter for MPPT via YYPO.

5. Case Studies

The proposed PoFoPID control is applied on a grid connected PV inverter to achieve MPPT under various atmospheric conditions, which control performance is compared to that of PID control [14], FoPID control [15], FLC [18], and SMC [33], under the following four scenarios, i.e., (a) Solar irradiation change; (b) Temperature variation; (c) Power grid voltage drop; and (d) Inverter parameter uncertainties. Besides, Table 1 gives the PV system parameters taken from reference [14], while a PV array of 30 panels in series is employed, in which each module owns 36 cells in series. In addition, the initial solar irradiation and temperature are set to be their rated values, e.g., 1 kW/m^2 and 25℃, respectively. Moreover, q-axis current I_q=0 for a unit power factor. Under this standard operation condition, the PV output power P=1867 W, DC link voltage V_{dc}=539.5 V, and PV output current I_{pv}=3.46 A, respectively.

The simulation is executed on Matlab/Simulink 7.10 using a personal computer with an Intel^R CoreTMi7 CPU at 2.2 GHz and 8 GB of RAM. Here, continuous time is used for the simulation with a fixed step size of 10^{-4} using ode4 (Runge-Kutta) solver. In addition, the three-level neutral-point-clamped VSC model for the PV inverter is adopted from Matlab/Simulink SimPowerSystems with insulated gate bipolar transistor (IGBT) and a switching

frequency of 1620 Hz, while this SimPowerSystems module automatically drives these switches. More detailed structure and parameters can be found in reference [34].

Table 1. The PV system parameters [14]

Typical peak power	60W	Factor of PV technology (A)	1.5
Voltage at peak power	17.1V	Series resistance	0.21Ω
Current at peak power	3.5A	Grid voltage (V:rms)	120V
Short-circuit current (I_{sc})	3.8A	Grid frequency (f)	50Hz
Open-circuit voltage (V_{oc})	21.1V	Grid inductance line (L)	2mH
Temperature coefficient of I_{sc} (k_1)	3mA/℃	Grid resistor line (R)	0.1Ω
Nominal operation cell temperature (T_{ref})	49℃	DC bus capacitor(C)	2200μF

5.1 Optimization results

For the purpose of a fair comparison, the control parameters of these five controllers are all optimally tuned by YYPO, which runs for 30 times and the best results, e.g., the control parameters corresponding to the lowest fitness function, are used and tabulated in Table 2. Furthermore, the statistical results are provided in Table 3, from which it can be seen that FLC requires the least convergence time as it has the fewest number of control parameters to be tuned. It is worth noting that FoPID control can obtain a lower fitness function than that of PID control thanks to the use of fractional-order mechanism. At last, PoFoPID control has the lowest fitness function thus it has the best control performance among all controllers. Note that all of these optimal control parameters are tuned offline due to the long computation time, once their optimal values are found they will be used in the corresponding controllers.

Table 2. The optimal control parameters of different controllers obtained by YYPO in 30 runs

Algorithm	q-axis current			DC-link voltage		
PID	$K_{P1} = 186$	$K_{I1} = 347$	$K_{D1} = 6$	$K_{P2} = 117$	$K_{I2} = 309$	$K_{D2} = 13$
FoPID	$K_{P1} = 164$	$K_{I1} = 314$	$K_{D1} = 4$	$K_{P2} = 131$	$K_{I2} = 277$	$K_{D2} = 5$
	$\mu_1 = 0.91$	$\lambda_1 = 1.83$		$\mu_2 = 1.62$	$\lambda_2 = 1.72$	
FLC	$\rho_{11} = 40$			$\rho_{21} = 15$	$\rho_{22} = 67$	
SMC	$\varsigma_1 = 9$	$\varphi_1 = 35$	$\varepsilon_{c1} = 0.2$	$\varsigma_2 = 15$	$\varphi_2 = 42$	$\varepsilon_{c2} = 0.2$
PoFoPID	$K_{P1} = 145$	$K_{I1} = 316$	$K_{D1} = 10$	$K_{P2} = 151$	$K_{I2} = 244$	$K_{D2} = 3$
	$\mu_1 = 0.67$	$\lambda_1 = 1.62$		$\mu_2 = 1.71$	$\lambda_2 = 1.46$	

Table 3. The statistical results of YYPO obtained by different controllers in 30 runs

Algorithm	Fitness function (p.u.)			Convergence time (hour)			Iteration number of convergence		
	Max.	Min.	Mean	Max.	Min.	Mean	Max.	Min.	Mean
PID	2.04	1.53	1.76	0.37	0.26	0.31	247	221	234
FoPID	1.76	1.35	1.47	0.42	0.33	0.39	278	251	266
FLC	1.22	1.04	1.13	0.11	0.06	0.08	89	61	72
SMC	1.30	1.11	1.19	0.24	0.13	0.18	137	119	128
PoFoPID	0.98	0.91	0.96	0.52	0.41	0.46	327	296	315

5.2 Solar irradiation change

Two consecutive step changes of solar irradiation are studied, which decreases from 1 kW/m² to 0.5 kW/m² at t=0.2 s and increases to 1 kW/m² at t=1.2 s, respectively. The temperature maintains at the rated value. Moreover, q-axis current I_q is increased to 50 A at t=0.2 s and is then decreased to -30 A at t=1.2 s and finally restored to 0 A at t=1.7 s. The corresponding system responses are demonstrated by Fig. 6, which shows that both the PID control and FoPID control have DC-link voltage oscillations while the other three nonlinear controllers have no such oscillations, this is due to the cancellation of PV system nonlinearities. In addition, it is clear that PoFoPID control can offer the most satisfactory control performance as it has the fastest tracking rate and the lowest overshoot in both DC-link voltage and q-axis current.
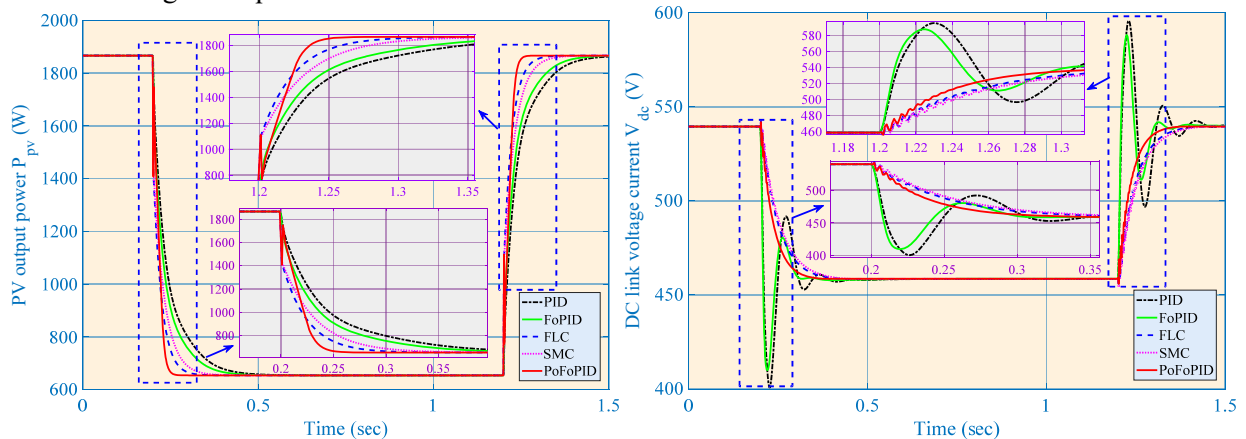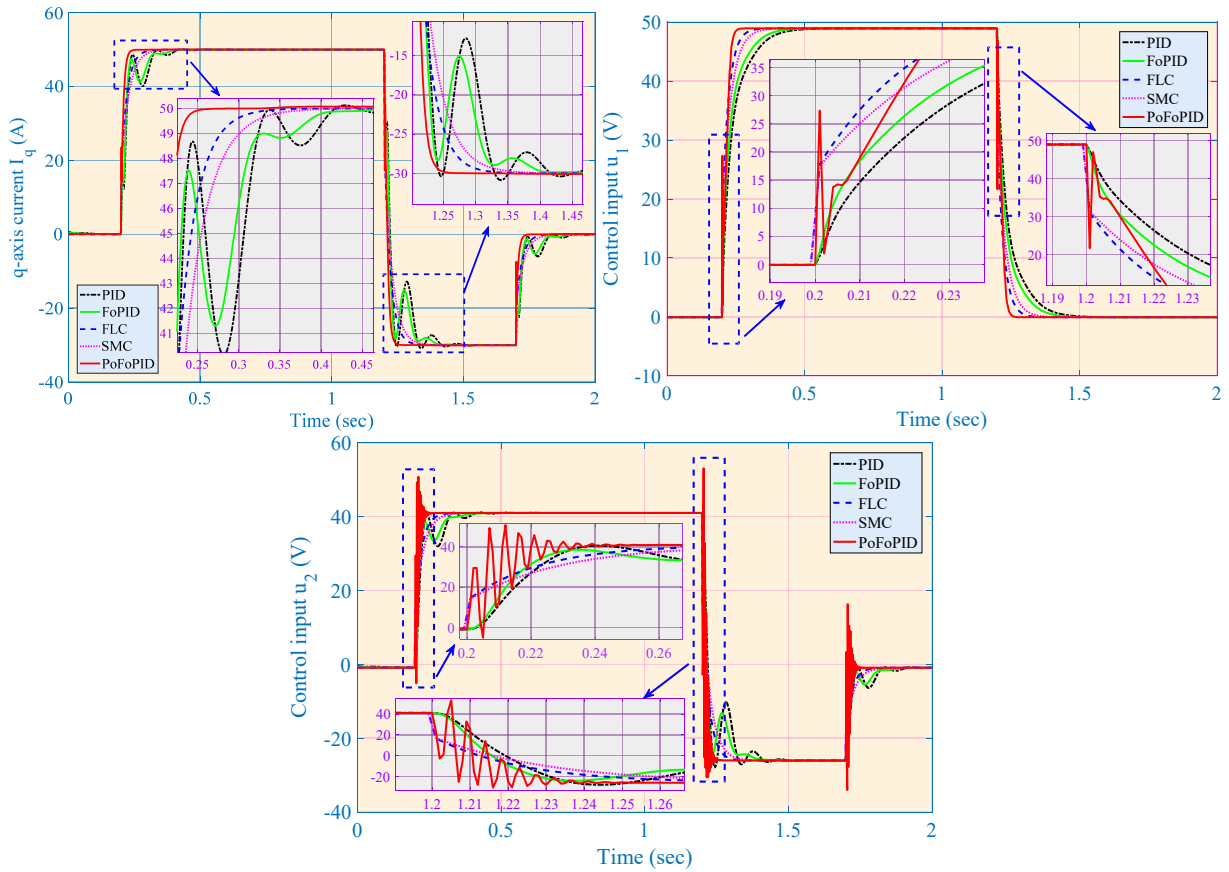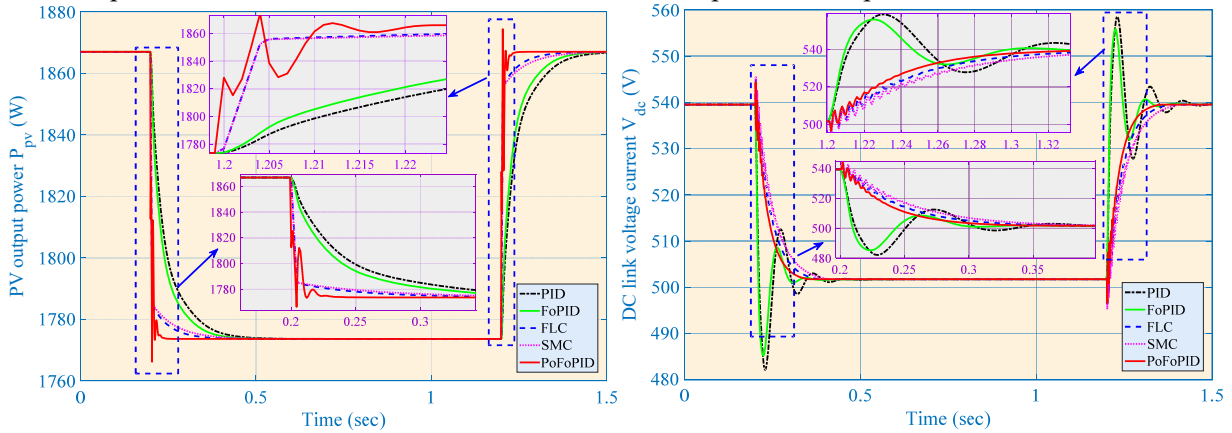
Figure 6. System responses obtained under solar irradiation change and q-axis current regulation.

5.3 Temperature variation

Two consecutive step changes of temperature are then investigated, e.g., at t=0.2 s the temperature increases from 25℃ to 40℃ and at t=1.2 s it reduces from 40℃ to 25℃, while the solar irradiation keeps at the rated value. Meanwhile, q-axis current I_q is decreased to -40 A at t=0.2 s and increased to 20 A at t=1.2 s and finally restored to 0 A at t=1.7 s. Figure 7 depicts the corresponding PV system responses, from which one could see that PoFoPID control can outperform the other controllers thanks to the full compensation of perturbation in the real-time.
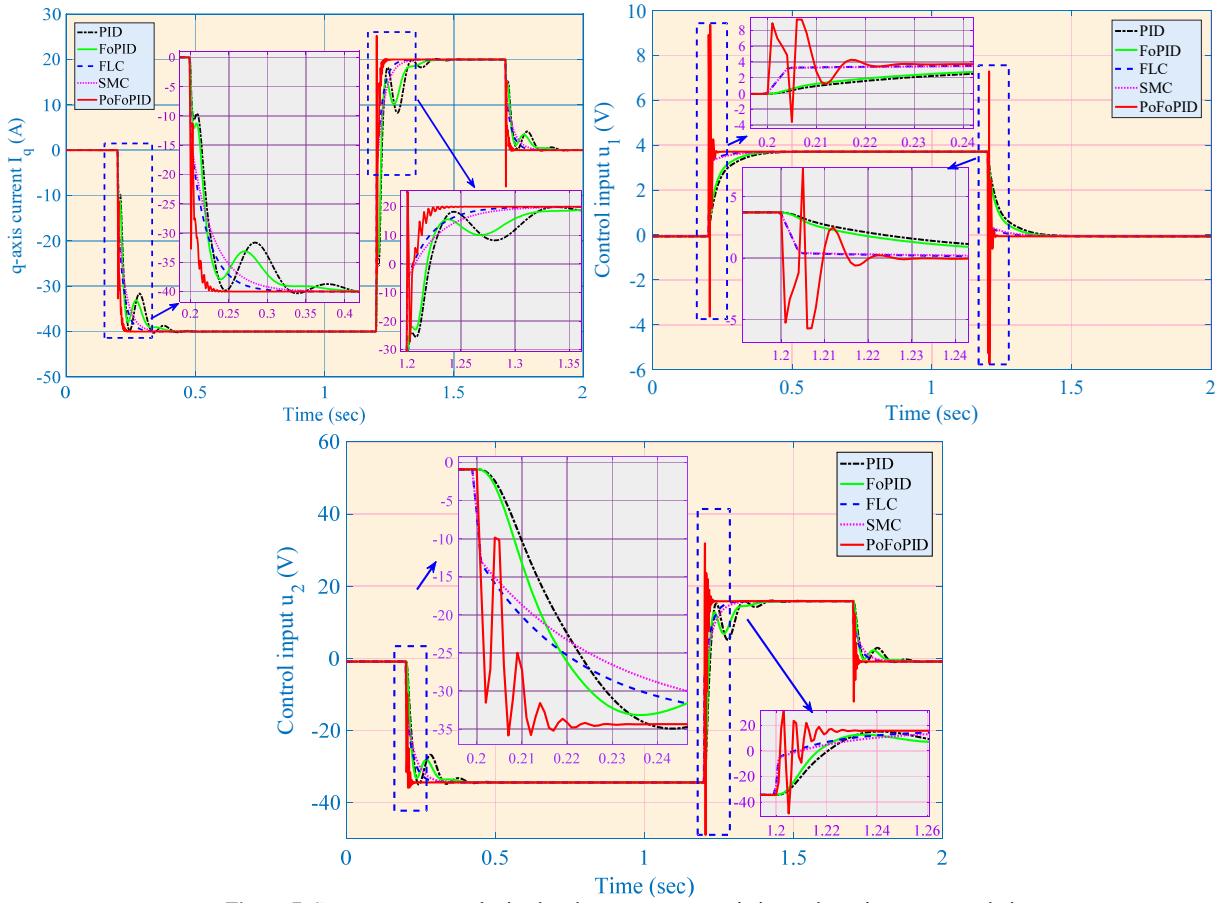
Figure 7. System responses obtained under temperature variation and q-axis current regulation.

5.4 Power grid voltage drop

In order to evaluate the fault-ride through (FRT) capability [35,36] of the PV system, a power grid voltage drop occurs at t=0.2 s to 0.4 p.u. and restores to the rated value at t=0.35s is tested. Figure 8 illustrates that PoFoPID control can effectively suppress the resulted power oscillations and can efficiently regulate the DC-link voltage with the fastest rate, thus it owns the highest FRT capability among all controllers. In contrast, PID presents the largest overshoot and slowest regulation rate.

Besides, the perturbation estimation performance of HGPO and HGSPO is also monitored during and after the power grid voltage drop, as shown in Fig. 9. It is obvious that the perturbation can be rapidly estimated which ensures the effectiveness of the online perturbation compensation.
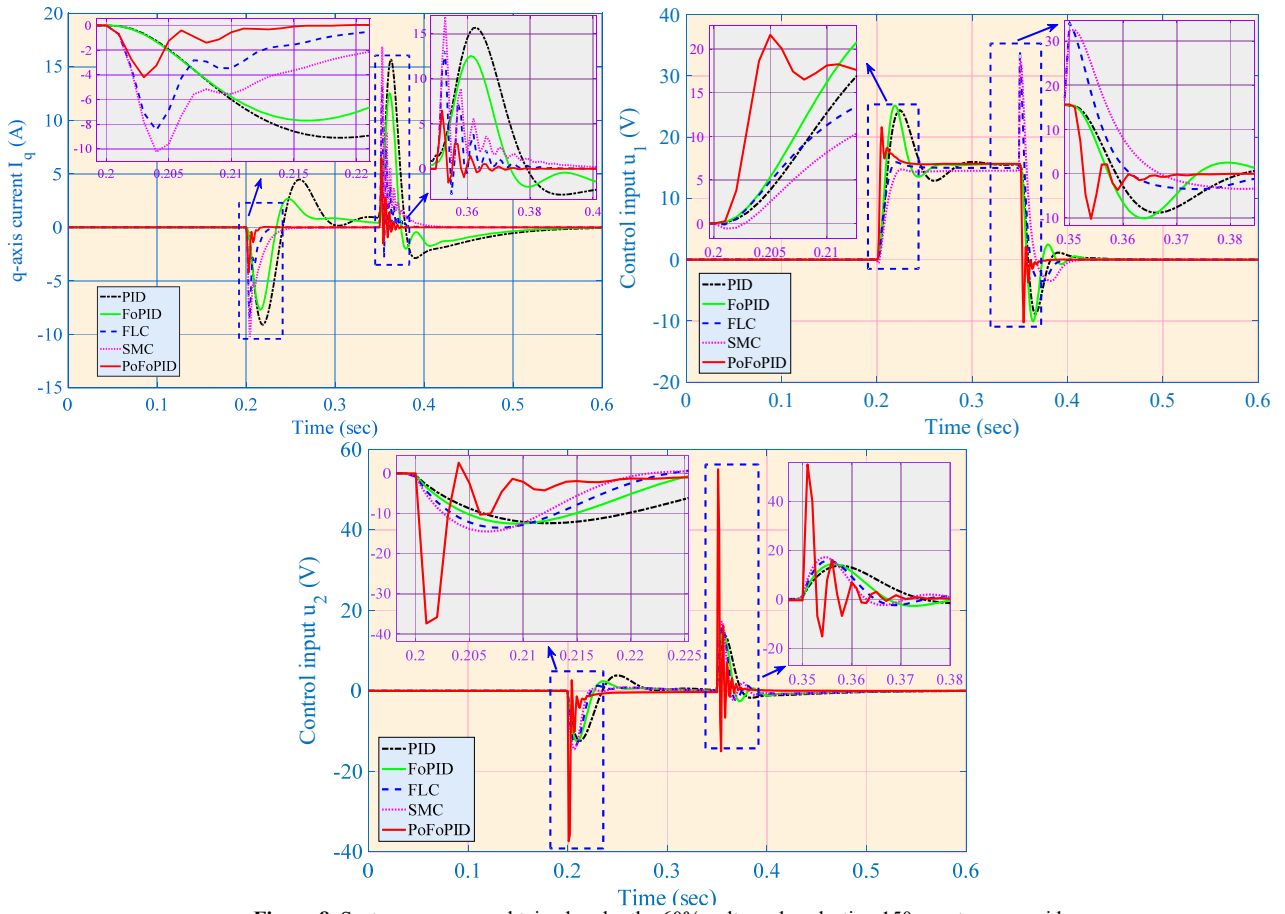

13
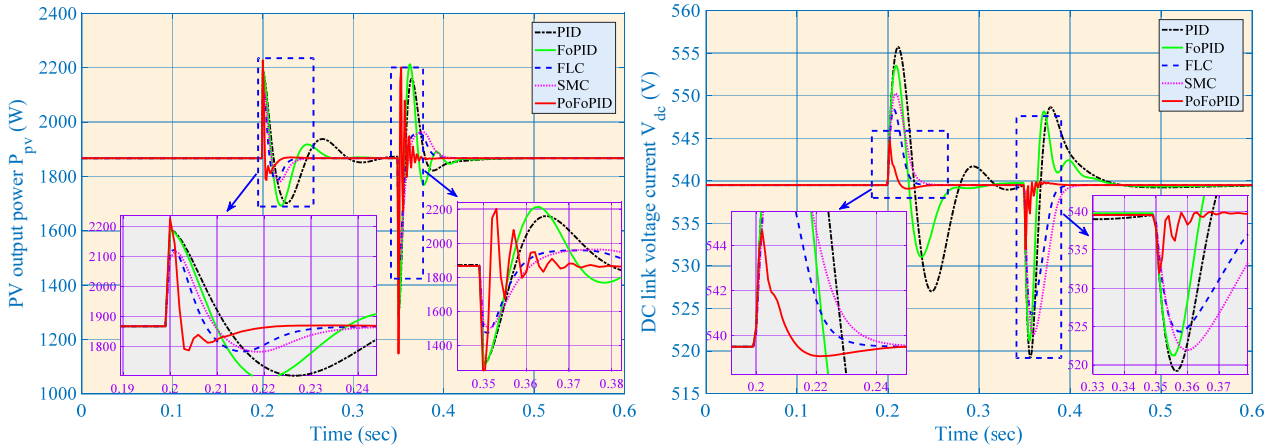
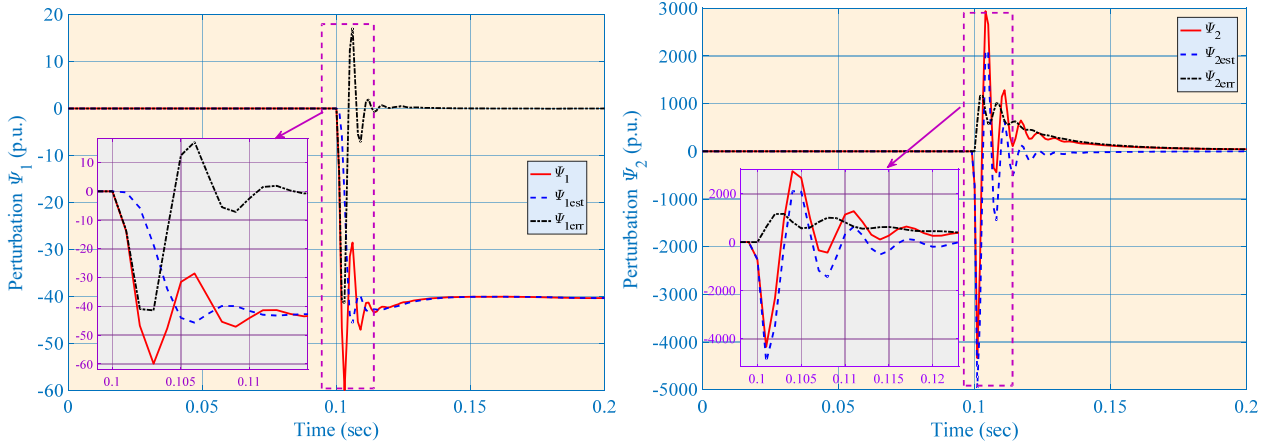**Figure 8.** System responses obtained under the 60% voltage drop lasting 150 ms at power grid.

Figure 9. Perturbation estimation performance of HGPO and HGSPO obtained under the 60% voltage drop lasting 150 ms at power grid.

5.5 Inverter parameter uncertainties

The robustness of PoFoPID control is compared to that of other methods in the presence of inverter parameter uncertainties. More specifically, a series of plant-model mismatches of the equivalent grid resistance R and grid inductance L with ±20% variation around their nominal value are carried out. Then, a 70% power grid voltage drop occurs which lasts 100 ms while the peak value of the active power $|P|$ is recorded. Figure 10 demonstrates that the variation of peak value of the active power $|P|$ obtained by PID control, FoPID control, FLC, SMC, and PoFoPID control is 42.7%, 39.2%, 71.5%, 22.9%, and 19.1%, respectively (which value is calculated by the difference between the maximum power value and minimum power value shown in Fig. 10). Consequently, PoFoPID control is able to provide the greatest robustness against to inverter parameter uncertainties, this is due to the real-time perturbation compensation, while FLC performance varies significantly as it is very sensitive to parameter uncertainties.
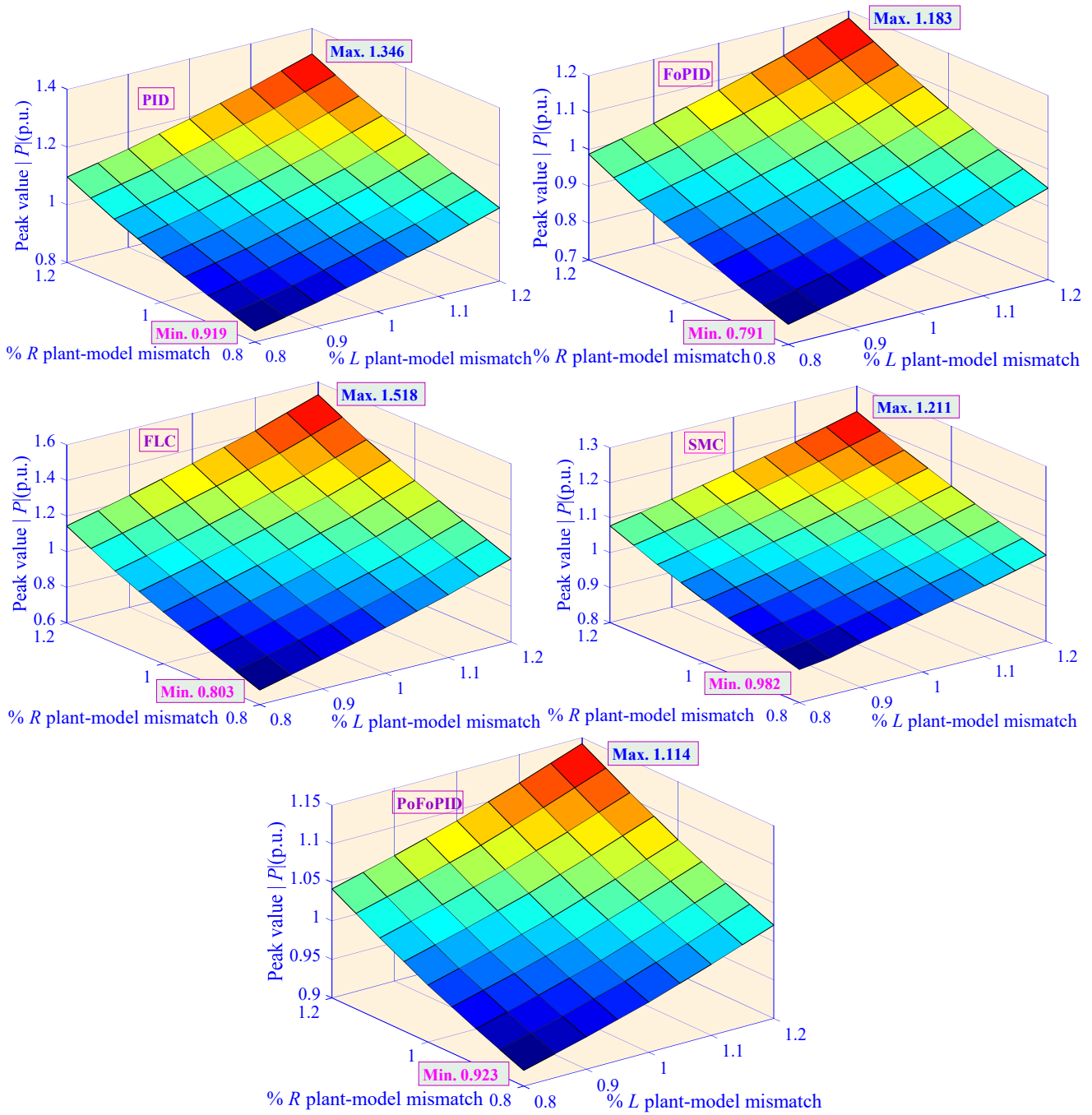
Figure 10. Peak value of active power |P| obtained under a 70% power grid voltage drop lasting 100 ms at power grid with 20% variation of the equivalent resistance R and inductance L of different controllers.

5.6 Comparative studies

The integral of absolute error (IAE) indices [37-40] of five controllers obtained in three cases are tabulated in Table 4. Here $IAE_x = \int_0^T |x - x^*| \, dt$, from which it shows that PoFoPID control owns the lowest IAE indices in all cases, which verifies that it can achieve the most satisfactory control performance among all approaches. More specifically, its IAE_{Iq} is only 61.54%, 65.74%, 76.53%, and 80.66% of that of PID control, FoPID control, FLC, and SMC in the temperature variation., respectively. Meanwhile, its IAE_{Vdc} is just 69.97%, 75.75%, 79.91%, and 83.91% of that of PID control, FoPID control, FLC, and SMC in the power grid voltage drop, respectively.

Table 4. IAE indices (in p.u.) of five controllers obtained in three cases

Cases	IAE Indices	PID	FoPID	FLC	SMC	PoFoPID
Solar irradiation change	IAE_{Iq}	0.1805	0.1776	0.1521	0.1415	0.1125
	IAE_{Vdc}	0.4521	0.4201	0.3928	0.3837	0.3496
Temperature variation	IAE_{Iq}	0.2257	0.2113	0.1815	0.1722	0.1389

	IAE$_{Vdc}$	0.5618	0.5387	0.5024	0.4918	0.4518
Power grid voltage drop	IAE$_{Iq}$	0.3439	0.3012	0.2698	0.2527	0.1966
	IAE$_{Vdc}$	0.7522	0.6948	0.6586	0.6272	0.5263

Morevoer, the overall control costs, i.e., $\int_0^T (|u_1| + |u_2|) \mathbf{d}t$ [41], of each controllers needed in three cases are compared in Fig. 11. It verifies that PoFoPID control only requires the minimal control costs in all cases among all controllers thanks to the combination of real-time perturbation compensation and FoPID control framework, which offers significant robustness as well as improved dynamic responses. In particular, its control costs needed in the power grid voltage drop are merely 90.97%, 93.41%, 96.98%, and 96.20% to that of PID control, FoPID control, FLC, and SMC, respectively. Note that SMC requires higher control costs than that of FLC as it employs the upper bound of perturbation which usually results in an over-conservativeness.
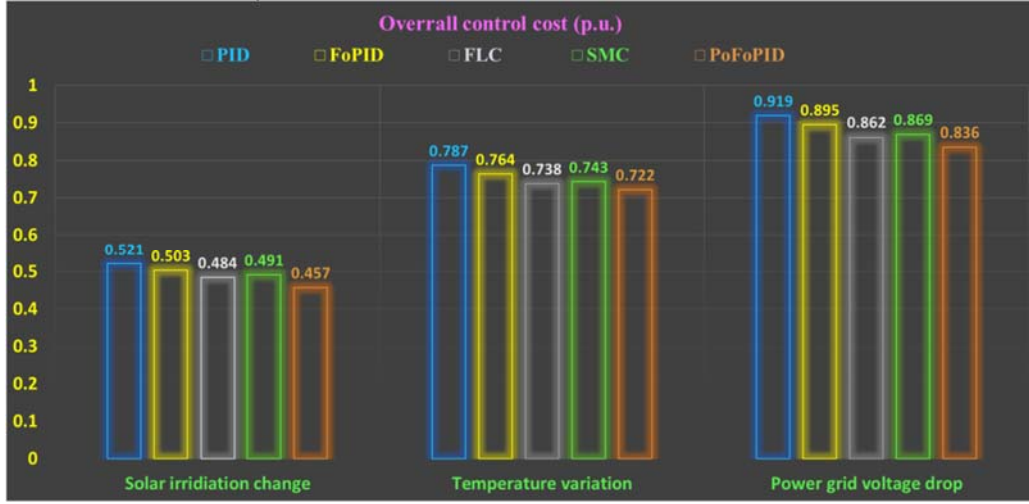

Figure 11. Overall control costs required by different controllers under three cases.

Lastly, the control performance of different controllers obtained in three cases is compared in Table 5. From which one can clearly see that FoPID can reduce the overshoot of DC-link voltage in the solar irradiation change by 5.64% and decrease the steady-state error by 7.69% compared to that of PID control thanks to the use of fractional-order mechanism. In addition, FLC can outperform SMC, e.g., 4.96% and 10% reduction of overhoot and steady-state error, in solar irradiation change, which is resulted from the over-conservativenss of SMC. Besides, PoFoPID owns the most satisfactory control performance thanks to the hybrid of real-time perturbation compensation and FoPID control framework. More specifically, its overhoot and steady-state error of DC-link voltage in the solar irradiation change is merely 75.65% and 66.67% to that of the second best controller (FLC). Similar conclusions can be obtained in other indices or cases from Table 5. To summarize, the nonlienar controllers (FLC, SMC, and PoFoPID control) can dramatically reduce the overshoot and steady-state error in comparison to that of linear controller (PID control and FoPID control) by the nonlinearities compensation. However, according to the 'No Free Lunch Theorem', they also result in a significant growth of controller structure complexity and computational burden. Note that althrough PoFoPID control has the most complicated structure compared to that of other approaches, it is practically applicable thanks to the fast development of modern control systems and the implementation feasibility will be studied in the following section.

Table 5. The control performance comparison of different controllers obtained in three cases (left/right number represents DC-link voltage/q-axis current results, respectively)

Cases	Algorithm	Rising time (ms)	Settling time (ms)	Maximum settling time (ms)	Minimum settling time (ms)	Overshoot (%)	Steady-state error (mV/mA)	Complexity level
Solar irradiation change	**PID**	38/52	227/220	56/68	102/111	14.38/1.62	13/2.2	Very Low
	FoPID	35/49	219/213	47/57	98/103	13.57/1.54	12/2	Low
	FLC	142/46	190/184	176/166	181/170	1.15/0.98	9/1.6	Medium
	SMC	156/48	195/187	181/170	187/176	1.21/1.03	10/1.9	High
	PoFoPID	118/44	175/178	164/167	168/171	0.87/0.64	6/1.5	Very high
Temperature variation	**PID**	42/55	235/228	51/63	102/117	4.09/1.55	15/2.6	Very Low
	FoPID	40/53	232/225	48/60	100/109	3.97/1.43	14/2.4	Low
	FLC	145/49	219/214	201/197	208/201	1.12/0.94	11/1.8	Medium
	SMC	159/51	224/218	213/202	219/207	1.17/0.98	12/2.1	High
	PoFoPID	121/46	201/208	186/191	193/198	0.82/0.61	8/1.7	Very high

	PID	15/13	165/235	18/16	54/76	2.98/1.12	9/1.5	Very Low
Power grid	FoPID	15/12	107/204	17/14	49/72	2.65/0.98	8/1.3	Low
voltage drop	FLC	10/8	57/41	13/10	47/32	1.63/0.53	5/0.9	Medium
	SMC	13/10	60/52	15/12	52/36	2.06/0.67	7/1.1	High
	PoFoPID	7/5	56/29	9/7	38/21	1.02/0.33	3/0.5	Very high

6. HIL Experiment

HIL experiment offers a crucial platform to evaluate and justify the complex real-time embedded systems through introducing the complexity of the controlled system to the test platform [42]. It has validated the implementation feasibility of different PV controllers systems [43-45].

A dSPACE based HIL experiment is carried out which configuration and experiment platform are presented in Fig. 12 and Fig. 13, respectively. In particular, PoFoPID controller (33) of q-axis current and DC-link voltage is embedded on one dSPACE platform (DS1104 board) with a sampling frequency f_c=1 kHz. Meanwhile, the PV system and INC based MPPT algorithm (1)-(8) is implemented on another dSPACE platform (DS1006 board) with a limit sampling frequency f_s= 50 kHz to make HIL simulator as close to the real PV system as possible [46]. Moreover, the q-axis current i_q and DC-link voltage V_{dc} are measured from the real-time simulation of the PV system on the DS1006 board, which are then transmitted to PoFoPID controller implemented on the DS1104 board for the real-time control inputs calculation. It is worth noting that the inverter circuits, sensors and other circuits are all embedded in DS1006 board.

The HIL experiment is undertaken in order to validate the hardware implementation feasibility of the proposed approach and to evaluate its real-time computation capability.
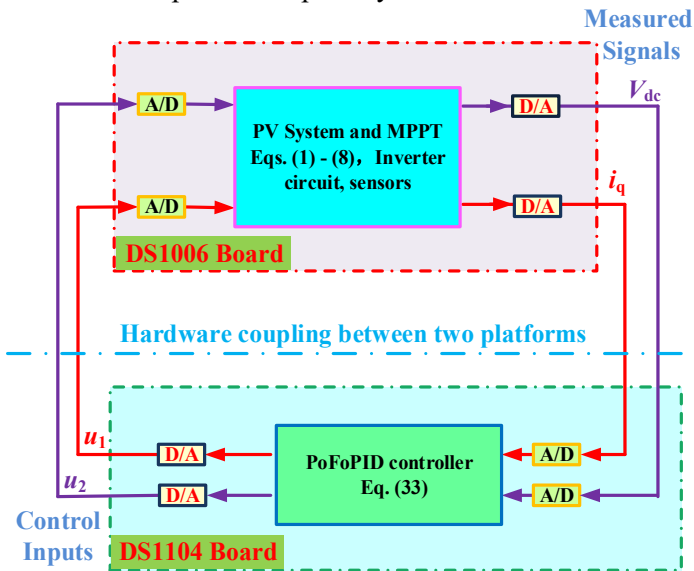

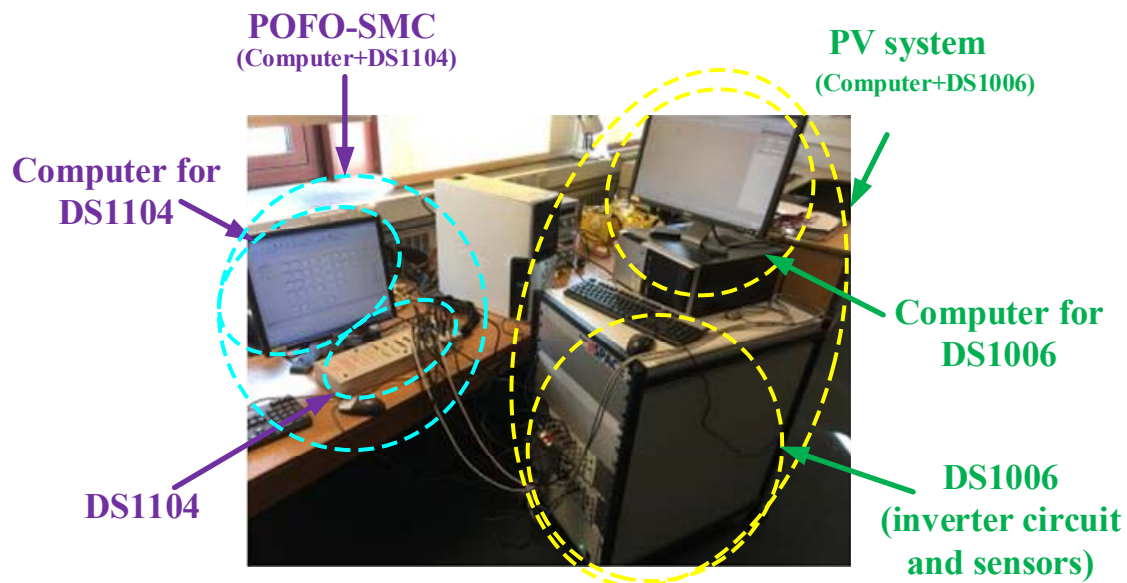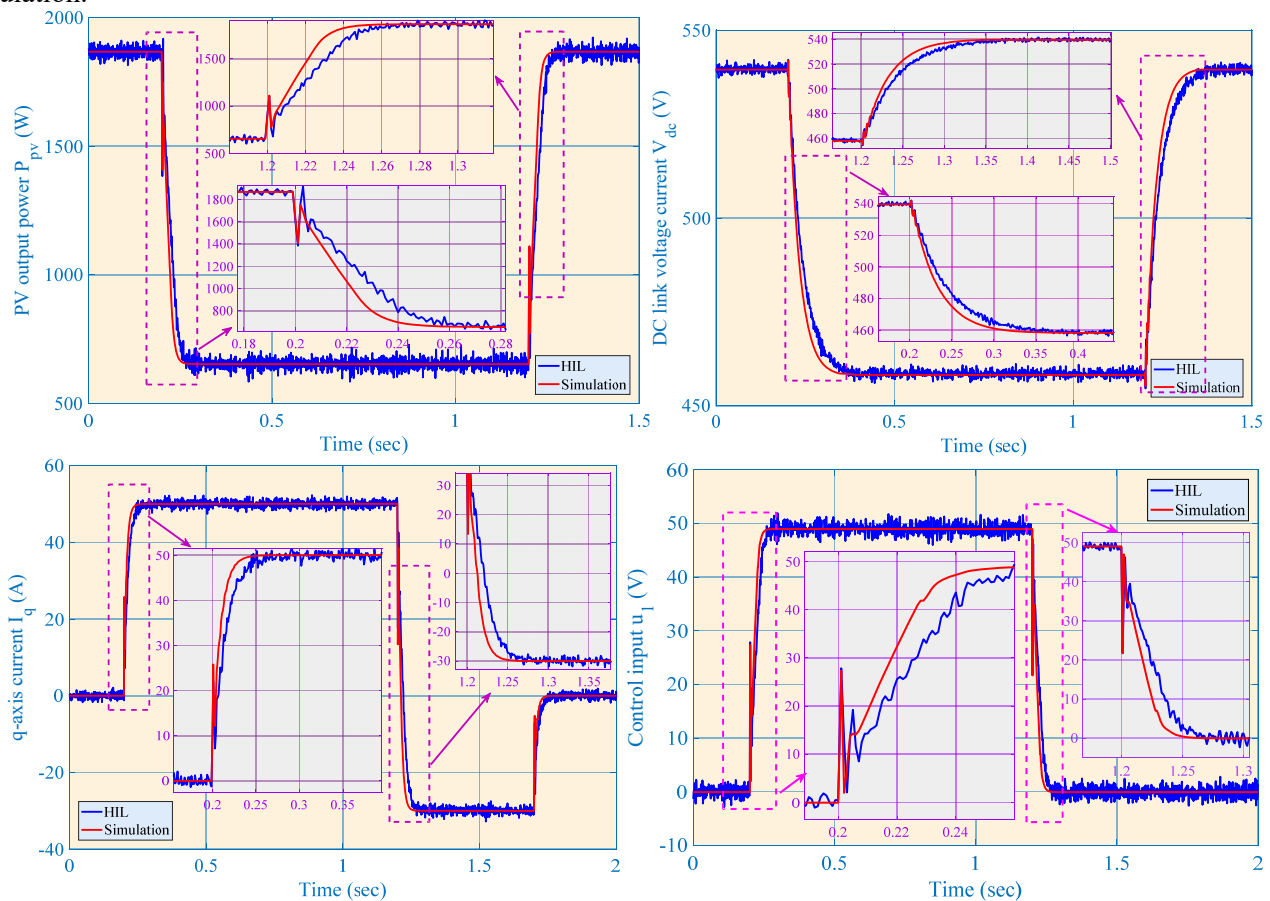**Figure 12.** The configuration of HIL experiment.

17

Figure 13. The hardware platform of HIL experiment.

6.1 Solar irradiation change

Figure 14 compares the system responses obtained by both the simulation and HIL experiment in the presence of the same solar irradiation change. It can be seen that HIL experiment results are quite similar to that of the simulation.
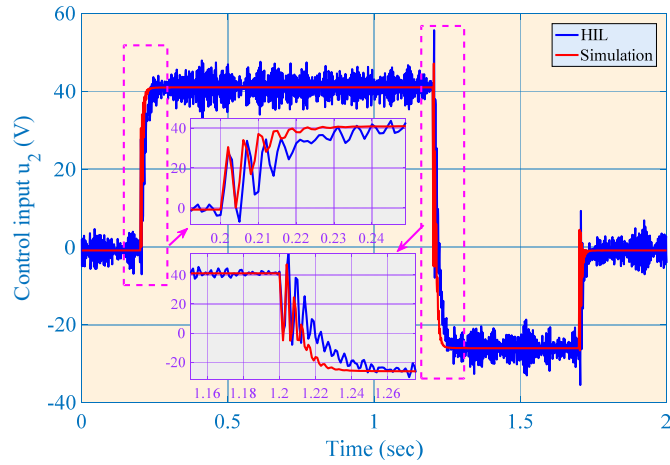
Figure 14. Simulation and HIL experiment results obtained under solar irradiation change and q-axis current regulation.

6.2 Temperature variation

Under the same scenario of temperature variation, Figure 15 illustrates that the MPPT performance of HIL experiment matches the simulation results very well.
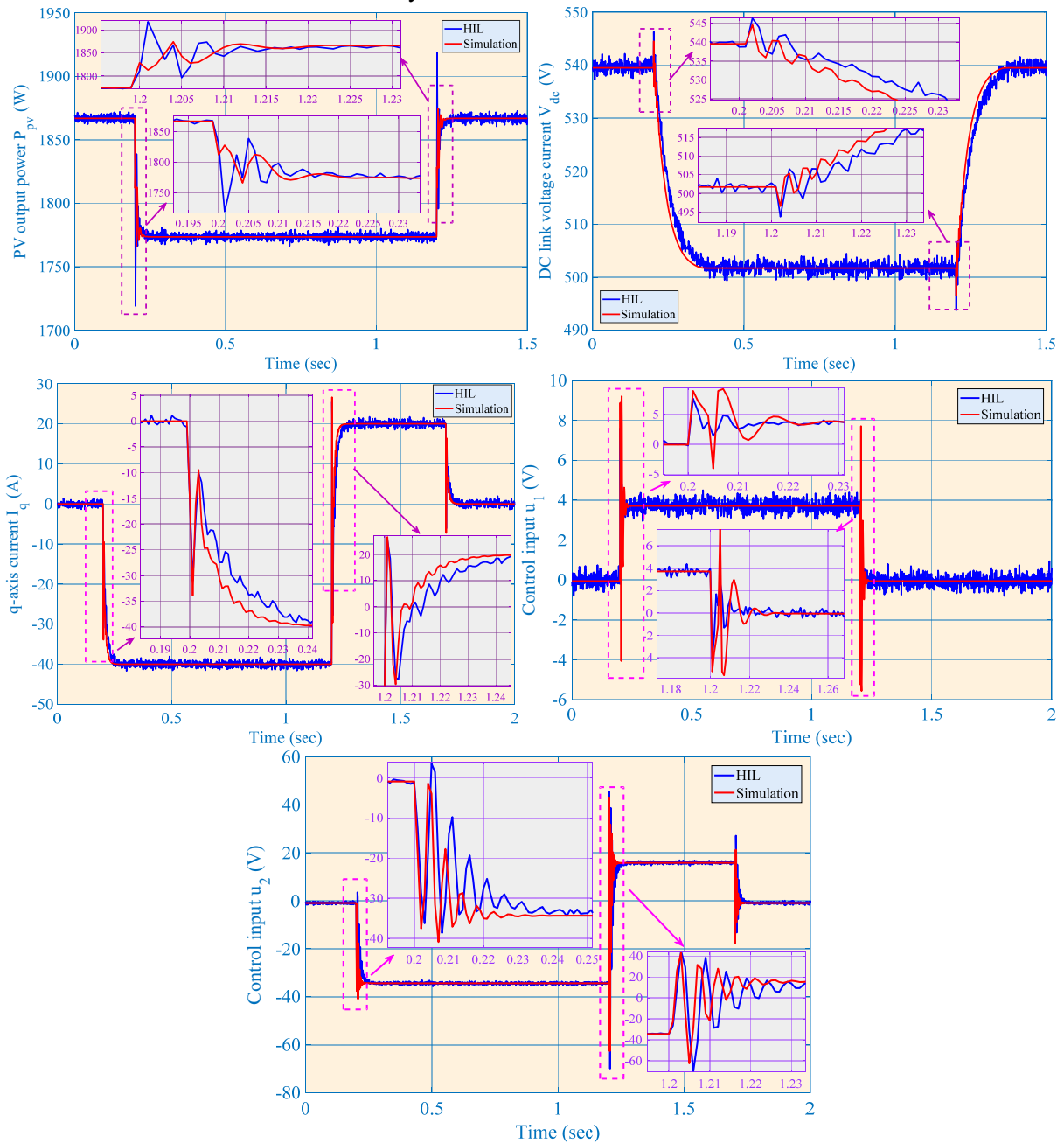

Figure 15. Simulation and HIL experiment results obtained under temperature variation and q-axis current regulation.

6.3 Power grid voltage drop

The same power grid voltage drop is applied while the corresponding results are given in Fig. 16, one can observe that the curve of HIL experiment and simulation is very close.
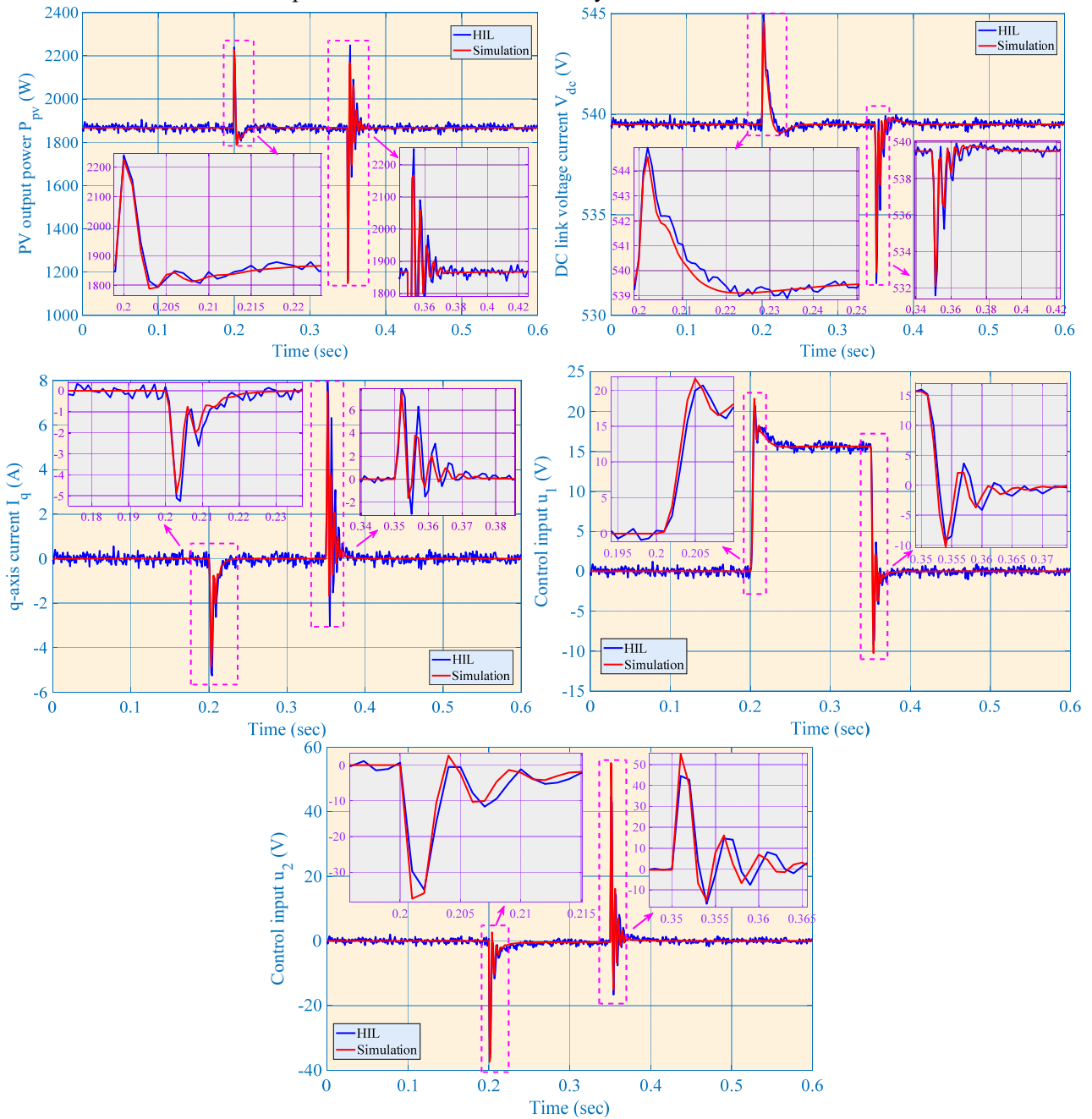

Figure 16. Simulation and HIL experiment results obtained under the 60% voltage drop lasting 150 ms at power grid.

To this end, the difference between the simulation results and HIL experiment results is mainly resulted from the following three factors:

• *Uncertain measurement disturbances and noises in the HIL experiment*: which is not considered in the simulation and mainly leads to the consistent oscillations of the HIL experiment results. A filter could be employed to noticeably attenuate such disturbances to improve the control performance;

• *Discretization of the HIL experiment and sampling holdin*g: which might bring an additional amount of trackinf errors compared to the continuous control adopted in the simulation;

• *Time delay of the real-time controll*er: which exact value is quite hard to acquire in HIL experiment. Such control signal transmission delay usually results in a degraded control performance, which can be seen from the HIL experiment results that they generally respond slightly slower than that of the simulation results.

7. Discussions

7.1 YYPO role, performance and properties

YYPO is remarkably simple and very flexible as it is derivative-free and does not require any prior knowledge on the physics of the problem. Moreover, YYPO is not a population-based algorithm, which utilizes two points instead of a population. Comprehensive studies have demonstrated that YYPO generally owns a significantly lower algorithm complexity compared to several typical meta-heuristic algorithms, e.g., artificial bee colony (ABC), ant-lion optimizer (ALO), differential evolution (DE), grey wolf optimizer (GWO), and particle swarm optimization (PSO), as well as some direct search algorithm, e.g., pattern search (PS) and multidirectional search (MDS). The self-adaptive nature of YYPO results in a nonlinear algorithm complexity with respect to problem dimension, which also enables YYPO to perform consistently over different problem dimensions for a noticeable number of problems. More details can be found in reference [27].

The need of YYPO is its user-defined parameters, which are the minimum and maximum number of archive updates I_{min} and I_{max} (both of which can assume integer values between 1 and maximum number of iteration, with $I_{min} \leq I_{max}$), and the expansion/contraction factor α (which should be given positive non-zero real values). The number of iterations after which the algorithm proceeds to the archive stage (I) is randomly generated within the bounds I_{min} and I_{max}. The parameter I also defines the maximum size of the archive, which is $2I$ (as two points are added to the archive at every iteration). In its simplest form, I may be given a fixed static value, resulting in a two parameters (I and α) algorithm. It can be inferred that, as δ_1 and δ_2 are varied inside the archive stage, I defines the frequency with which the δ_1 and δ_2 values are decreased and increased, respectively. The extent to which they are changed is defined by the other user-defined parameter α, as can be noted from Eq. (22). A large value of α will result in smaller changes in δ values and vice versa. Thus, it is apparent that α and I are interdependent, as a high or low value of both α and I simultaneously would potentially result in poor performance of the algorithm. More specifically, the first case would lead to δ_1 and δ_2 undergoing small changes infrequently, while the second case would lead to a large and frequent fluctuations [27].

Besides, the optimization problem of this paper is a single-objective optimization, which has been effectively resolved by YYPO. In fact, YYPO has been extended into multiple-objective optimization in reference [28], which is called front-based Yin-Yang-Pair optimization (F-YYPO). F-YYPO just requires the same user-defined parameters to that of YYPO. More detailed design and analysis can be referred in literature [28] for interested readers.

7.2 Partial shading conditions

It is worth noting that the PoFoPID control is designed for PV inverter, when the optimal DC-link voltage is obtained, PoFoPID control can regulate the DC-link voltage to that reference effectively and efficiently. Hence, PoFoPID control is independent to global search of MPPs. In other words, it is able to satisfactorily track the MPP no matter whether it is a global MPP or a local MPP. In this work, only the uniform solar irradiation condition is considered, which has only a single global MPP searched by INC technique. Thus, PoFoPID control can achieve the global MPPT.

However, non-uniform solar irradiation conditions, that is, partial shading condition, may emerge where the solar irradiation is unequally distributed among the PV modules, while each PV module can be exposed to different solar irradiation due to the shadows of buildings, trees, clouds, birds, dirt, etc.[47-49]. Under such scenario, the resulting *P-V* curve usually have multiple local peaks and single global peak due to bypass diode. INC technique or P&O method may not be able to seek the global MPP and be easily trapped at a local MPP. To handle such challenge, YYPO will be employed in the global MPP search instead of INC technique, which searching performance is compared to that of INC technique. As explained above, the global MPP search and DC-link reference tracking are independent, thus only the MPP search results have been provided. Once the global MPP is found by YYPO, PoFoPID control will rapidly regulate the DC-link voltage to that reference, as seen from the case studies provided in Section 5.

Three series-connected LA361K51S PV modules are adopted in Matlab/Simulink environment. Its operation scenario is based on sensing shaded PV voltage and current that are fed to MPPT block to search duty cycle at which global maximum power can be derived [49]. Figure 17 illustrates the MPPT performance obtained under partial shading conditions by INC technique and YYPO, which contains a single global MPP and two local MPPs. It can be clearly observed that INC technique is trapped at a local MPP which can only generate a power of 1258 W within t_2=28 ms as it has no local MPP avoidance mechanism. In contrast, YYPO could effectively seek the global MPP and can extract the available maximum power of 1867 W within t_1=65 ms. The longer convergence time t_1 shows that YYPO undertakes a wider searching to ensure a global MPP. Meanwhile, the power oscillations exhibited in the initial phase of YYPO clearly demonstrate its exploration mechanism, which avoids YYPO to be trapped at the local MPP.
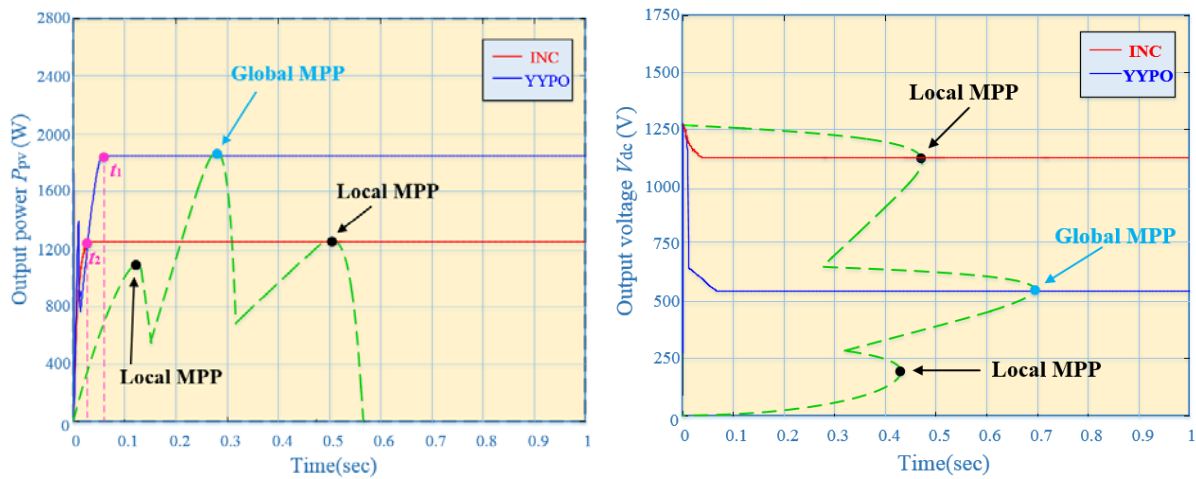
Figure 17. MPPT performance obtained under partial shading conditions (one global MPP and two local MPP) by INC technique and YYPO.

8. Conclusions

This paper develops a novel PoFoPID controller for grid-connected PV inverter to harvest the available maximum solar energy under various atmospheric conditions via YYPO. The main findings and conclusions can be summarized as follows:

(1) An HGSPO is used to efficiently estimate the aggregated effect of PV inverter nonlinearities, parameter uncertainties, unmodelled dynamics, stochastic fluctuation of atmospheric conditions, and external disturbances. Then, the perturbation estimate is fully compensated by the controller to realize a global control consistency as well as to noticeably enhance the system robustness;

(2) The FoPID control framework is incorporated in the controller design, such that improved dynamical responses of the closed-loop system can be achieved. Moreover, it is easy to be understood and accepted by the industry with relatively simple structure and high reliability;

(3) A meta-heuristic algorithm called YYPO inspired from the dualities in nature is employed to rapidly tune the optimal PoFoPID controller parameters, which ensures an optimal control performance under different cases. Besides, only the measurement of DC link voltage and q-axis current is required;

(4) Simulation results of case studies verify that PoFoPID controller can offer the most satisfactory control performance in terms of the lowest tracking error and fastest tracking rate, together with the minimal overall control costs against that of other four controllers;

(5) A dSpace based HIL experiment is carried out which validates the implementation feasibility of the proposed approach.

Future study will employ a real PV inverter and PV panel to carry out a hardware experiment to further validate the effectiveness of PoFoPID controller.

Acknowledgments

References

[1] Yang, B.; Zhang, X.S.; Yu, T.; Shu, H.C.; Fang, Z.H. Grouped grey wolf optimizer for maximum power point tracking of doubly-fed induction generator based wind turbine. *Energy Conversion and Management* **2017**, 133: 427-443.

[2] Yang, B.; Jiang, L.; Wang, L.; Yao, W.; Wu, Q.H. Nonlinear maximum power point tracking control and modal analysis of DFIG based wind turbine. *International Journal of Electrical Power & Energy Systems* **2016**, 74: 429-436.

[3] Shen, Y.; Yao, W.; Wen, J.Y.; He, H.B. Adaptive wide-area power oscillation damper design for photovoltaic plant considering delay compensation. *IET Generation, Transmission and Distribution* **2017**, 11(18): 4511-4519.

[4] Nojavan, S.; Majidi, M.; Zare, K. Performance improvement of a battery/PV/fuel cell/grid hybrid energy system considering load uncertainty modeling using IGDT. *Energy Conversion and Management* **2017**, 147: 29-39.

[5] Saravanan, S. and Babu, N. R. RBFN based MPPT algorithm for PV system with high step up converter. *Energy Conversion and Management* **2016**, 122: 239-251.

[6] Kandemir, E.; Cetin, N.S.; Borekci, S. A comprehensive overview of maximum power extraction methods for PV systems. *Renewable and Sustainable Energy Reviews* **2017**, 78: 93-112.

[7] Ahmed, J.; Salam, Z. An improved perturb and observe (P&O) maximum power point tracking (MPPT) algorithm for higher efficiency. *Applied Energy* **2015**, 150: 97-108.

[8] Al-Dhaifallah M.; Nassef A. M.; Rezk H.; Nisar K. S. Optimal parameter design of fractional order control based INC-MPPT for PV system. *Solar Energy* **2018**, 159: 650-664.

[9]   Ishaque, K. and Salam, Z. A deterministic particle swarm optimization maximum power point tracker for photovoltaic system under partial shading condition. *IEEE Transactions on Industrial Electronics* **2013**, 60(8): 3195-3206.

[10]   Ahmed, J. and Salam, Z. A Maximum Power Point Tracking (MPPT) for PV system using Cuckoo Search with partial shading capability. *Applied Energy* **2014**, 119: 118-130.

[11]   Mancilla, D.F.; Riganti-Fulginei, F.; Laudani, A.; Salvini, A. A neural network based low-cost solar irradiance sensor. *IEEE Transactions on Instrumentation and Measurement* **2014**, 63(3): 583-591.

[12]   Lauria, D.; Coppola, M. Design and control of an advanced PV inverter. *Solar Energy* **2014**, 110: 533-542.

[13]   Dash, P.P.; Kazerani, M. Dynamic modelling and performance analysis of a grid-connected current-source inverter based photovoltaic system. *IEEE Transactions on Sustainable Energy* **2011**, 2(4): 443-450.

[14]   Kadri, R.; Gaubert, J.P.; Champenois, G. An improved maximum power point tracking for photovoltaic grid-connected inverter based on voltage-oriented control. *IEEE Transactions on Industrial Electronics* **2011**, 58(1): 66-75.

[15]   Malek, H.; Dadras, S.; Chen, Y.Q. Application of fractional order current controller in three phase grid-connected PV systems. 2014 American Control Conference (ACC), June 4-6, **2014**. Portland, Oregon, USA, p. 5224-5229.

[16]   Mitkowski, W.; Oprzedkiewicz, K. Tuning of the half-order robust PID controller dedicated to oriented PV system. *Lecture Notes in Electrical Engineering* **2015**, 320: 145-157.

[17]   Ramadan, H.S. Optimal fractional order PI control applicability for enhanced dynamic behavior of on-grid solar PV systems. *International Journal of Hydrogen Energy* **2017**, 42(7): 4017-4031.

[18]   Lalili, D.; Mellit, A.; Lourci, N.; Medjahed, B.; Berkouk, E.M. Input output feedback linearization control and variable step size MPPT algorithm of a grid-connected photovoltaic inverter. *Renewable Energy* **2011**, 36: 3282-3291.

[19]   Lalili, D.; Mellit, A.; Lourci, N.; Medjahed, B.; Boubakir, C. State feedback control and variable step size MPPT algorithm of three-level grid-connected photovoltaic inverter. *Solar Energy* **2013**, 98: 561-571.

[20]   Mahmud, M.A.; Pota, H.R.; Hossain, M.J.; Roy, N.K. Robust partial feedback linearizing stabilization scheme for three-phase grid-connected photovoltaic systems. *IEEE Journal of Photovoltaics* **2013**, 4(1): 423-431.

[21]   Chatrenour, N.; Razmi, H.; Doagou-Mojarrad, H. Improved double integral sliding mode MPPT controller based parameter estimation for a stand-alone photovoltaic system. *Energy Conversion and Management* **2017**, 139: 97-109.

[22]   Naghmasha, Armghan, H.; Ahmad, Iftikhar.; Armghan, Ammar.; Khan, Saud.; Arsalan, Muhammad. Backstepping based non-linear control for maximum power point tracking in photovoltaic system. *Solar Energy* **2018**, 159: 134-141.

[23]   Tang, R. L.; Wu, Z.; Fang, Y. J. Configuration of marine photovoltaic system and its MPPT using model predictive control. *Solar Energy* **2017**, 158: 995-1005.

[24]   Mohomad, H.; Saleh, S.A.M.; Chang, L. Disturbance estimator-based predictive current controller for single-phase interconnected PV systems. *IEEE Transactions on Industry Applications* **2017**, 53(5): 4201-4209.

[25]   Yang, J., Chen, W.H., Li, S.H., Guo, L., Yan, Y.D. Disturbance/Uncertainty estimation and attenuation techniques in PMSM drives-A survey, *IEEE Transactions on Industrial Electronics* **2017**, 64 (4): 3273-3285.

[26]   Tam, S.C.; Chio, C.H.; Tam, H.K. Development of a new optimization method, yin-yang algorithm, for traveling salesman problem. International Conference on System Science and Engineering. IEEE, **2011**, p. 245-250.

[27]   Punnathanam, V. and Kotecha, P. Yin-Yang-pair Optimization: A novel lightweight optimization algorithm. *Engineering Applications of Artificial Intelligence* **2016**, 54: 62-79.

[28]   Punnathanam, V. and Kotecha, P. Multi-objective optimization of Stirling engine systems using Front-based Yin-Yang-Pair Optimization. *Energy Conversion and Managemen*t **2017**, 133: 332-348.

[29]   Yang, B.; Jiang, L.; Yao, W.; Wu, Q. H. Perturbation estimation based coordinated adaptive passive control for multimachine power systems. *Control Engineering Practice* **2015**, 44: 172-192.

[30]   Yang, B.; Jiang, L.; Yao, W.; Wu, Q. H. Perturbation observer based adaptive passive control for damping improvement of VSC-MTDC systems. *Transactions of the Institute of Measurement and Control* **2017**, 39(9): 1409-1420.

[31]   Yang, B.; Jiang, L.; Zhang, C.K.; Sang, Y.Y.; Yu, T.; Wu, Q.H. Perturbation observer based adaptive passive control for nonlinear systems with uncertainties and disturbances. *Transactions of the Institute of Measurement and Control* **2018**, 40(4): 1223-1236.

[32]   Podlubny, I. Fractional differential equations, Academic Press, New York, 1999.

[33]   Farhat, M.; Barambones, O.; Sbita, L. A new maximum power point method based on a sliding mode approach for solar energy harvesting. *Applied Energy* **2017**, 185(2): 1185-1198.

[34]   Li, S.; Haskew, T.A.; Xu, L. Control of HVDC light system using conventional and direct current vector control approaches. *IEEE Transactions on Power Electronics* **2010**, 25(12): 3106-3118.

[35]   Wang, Y.; Ren, B. Fault ride-through enhancement for grid-tied PV systems with robust control. *IEEE Transactions on Industrial Electronics* **2018**, 65(3): 2302-2312.

[36]   Hasanien, H.M. An adaptive control strategy for low voltage ride through capability enhancement of grid-connected photovoltaic power plants. *IEEE Transactions on Power Systems* **2016**, 31(4): 3230-3237.

[37]   Yao, W.; Jiang, L.; Wen, J.Y.; Wu, Q.H.; Cheng, S.J. Wide-area damping controller for power system inter-area oscillations: a networked predictive control approach. *IEEE Transactions on Control Systems Technology* **2015**, 23(1): 27-36.

[38]   Shen, Y.; Yao, W.; Wen, J.Y.; He, H.B.; Chen, W.B. Adaptive supplementary damping control of VSC-HVDC for interarea oscillation using GrHDP. *IEEE Transactions on Power Systems* **2018**, 33(2): 1777-1789.

[39]   Liao, S.W.; Yao, W.; Han, X.N.; Wen, J.Y.; Cheng, S.J. Chronological operation simulation framework for regional power system under high penetration of renewable energy using meteorological data. *Applied Energy* **2017**, 203: 816-828.

[40]   Liu, J.; Wen, J.Y.; Yao, W.; Long, Y. Solution to short-term frequency response of wind farms by using energy storage systems. *IET Renewable Power Generation* **2016**, 10(5): 669-678.

[41]   Yang, B.; Yu, T.; Shu, H.C.; Zhang, X.S.; Qu, K.P.; Jiang, L. Democratic joint operations algorithm for optimal power extraction of PMSG based wind energy conversion system. *Energy Conversion and Management* **2018**, 159:312-326, 2018.

[42]   Tremblay, O.; Fortin-Blanchette, H.; Gagnon, R.; Brissette, Y. Contribution to stability analysis of power hardware-in-the-loop simulators. *IET Generation Transmission & Distribution* **2017**, 11(12): 3073-3079.

[43]   Rezkallah, M.; Hamadi, A.; Chandra, A.; Singh, B. Real-time HIL implementation of sliding mode control for standalone system based on PV array without using dumpload. *IEEE Transactions on Sustainable Energy* **2015**, 6(4): 1389-1398.

[44]   Jung, J.H. Power hardware-in-the-loop simulation (PHILS) of photovoltaic power generation using real-time simulation techniques and

power interfaces. *Journal of Power Source*s **2015**, 285: 137-145.

[45] Mai, X.H.; Kwak, S.K.; Jung, J.H.; Kim, K.A. Comprehensive electric-thermal photovoltaic modeling for power-hardware-in-the-loop simulation (PHILS) applications. *IEEE Transactions on Industrial Electronics* **2017**, 64(8): 6255-6264.

[46] Yang, B.; Yu, T.; Shu, H.C.; Zhang, Y.M.; Chen, J.; Sang, Y.Y.; Jiang, L. Passivity-based sliding-mode control design for optimal power extraction of a PMSG based variable speed wind turbine, *Renewable Energy* **2018**, 119: 577-589.

[47] Benyoucef, A.S.; Chouder, A.; Kara, K.; Silvertre, S.; Sahed, O.A. Artificial bee colony based algorithm for maximum power point tracking (MPPT) for PV systems operating under partial shaded conditions. *Applied Soft Computing* **2015**, 32: 38-48.

[48] Bizon N. Global extremum seeking control of the power generated by a photovoltaic array under partially shaded conditions. *Energy Conversion and Management* **2016**, 109: 71-85.

[49] Rezk H.; Fathy A.; Abdelaziz. A.Y. A comparison of different global MPPT techniques based on meta-heuristic algorithms for photovoltaic system subjected to partial shading conditions. *Renewable and Sustainable Energy Reviews* **2017**, 74:377-386.